



# Influence of $Zn^{2+}$ ions on the structural and electrical properties of $Mg_{1-x}Zn_xFeCrO_4$ spinels



K.A.M. Khalaf <sup>a,\*</sup>, A.D. Al-Rawas <sup>b</sup>, H.M. Widatallah <sup>b</sup>, K.S. Al-Rashdi <sup>b</sup>, A. Sellai <sup>b</sup>,  
A.M. Gismelseed <sup>b</sup>, Mohd Hashim <sup>c</sup>, S.K. Jameel <sup>d</sup>, M.S. Al-Ruqeishi <sup>b</sup>, K.O. Al-Riyami <sup>e</sup>,  
M. Shongwe <sup>f</sup>, A.H. Al-Rajhi <sup>g</sup>

<sup>a</sup> Department of Mathematical and Physical Sciences, College of Arts and Sciences, University of Nizwa, P.O. Box 33, Code 616, Oman

<sup>b</sup> Department of Physics, College of Science, Sultan Qaboos University, P.O. Box 36, Code 123, Oman

<sup>c</sup> Department of Physics, Aligarh Muslim University, Aligarh, 202002, India

<sup>d</sup> Al-Mustansiriyah University, College of Science, Department of Physics, Baghdad, Iraq

<sup>e</sup> Daris Research Center, University of Nizwa, P.O. Box 33, Code 616, Oman

<sup>f</sup> Department of Chemistry, College of Science, Sultan Qaboos University, P.O. Box 36, Code 123, Oman

<sup>g</sup> Department of Applied Science Curriculum Development, Ministry of Education, Oman

## ARTICLE INFO

### Article history:

Received 5 August 2015

Received in revised form

3 October 2015

Accepted 18 October 2015

Available online 21 October 2015

### Keywords:

Mg–Zn–Cr spinels

IR

XRD

TEM

SEM

EDS

TGA

DTA

Vacancy model

## ABSTRACT

The polycrystalline magnesium–zinc ferrite chromate having the chemical formula  $Mg_{1-x}Zn_xFeCrO_4$  ( $0.0 \leq x \leq 1.0$ ) were prepared by conventional solid phase reaction using high purity reagents. The structural and electrical properties at room temperature have been investigated by XRD, TEM, SEM, EDS, TGA, DTA, FT-IR and DC electrical resistivity techniques. The lattice parameters such as the lattice constant, average particle size, bonds length, density, porosity and volume shrinkage were found to vary with increasing  $Zn^{2+}$  content in the sample. The lattice constant “a” increases from 8.361 Å for  $MgFeCrO_4$  to 8.382 Å for  $ZnFeCrO_4$  spinels. The IR spectra confirm the presence of two main absorption bands  $\nu_1$  and  $\nu_2$  in the frequency range of 400–1000  $cm^{-1}$ , arising due to the tetrahedral (A) and octahedral (B) stretching vibrations respectively. Values of  $\nu_1$  and  $\nu_2$  decrease with increasing  $Zn^{2+}$  content over the whole composition range. The scanning electron microscope (SEM) and transmission electron microscope (TEM) micrographs showed aggregates of stacked large grains. Values of the room temperature DC electrical resistivity decrease as  $Zn^{2+}$  content increases. The low values of the vacancy model parameters indicate that the  $Mg_{1-x}Zn_xFeCrO_4$  spinels are strongly defective and the participation of the  $Zn^{2+}$  vacancies in the improvement of the electrical conductivity in these spinels. The thermo-gravimetric, TGA and differential thermal analysis, DTA show loss of mass caused by vaporization of the surface and trapped water molecules at higher temperatures.

© 2015 Elsevier B.V. All rights reserved.

## 1. Introduction

Spinel ferrites are insulating magnetic oxides. They have been the subject of extensive research because of their high permeability, moderate permittivity, high resistivity and low eddy current losses, which make them very useful in many technological applications [1–3] such as information storage systems, gas sensors, microwave devices and magnetic recording media and electronic industries. The electrical, magnetic, thermal and mechanical

properties of these materials depend strongly on their structural, dielectric and magnetic properties, which have been influenced by the method of preparation and heat treatment. Spinel ferrites are multi element oxide having the general formula  $AB_2O_4$ , where A and B represent the tetrahedral and octahedral complexes. The substitutions of various magnetic and non-magnetic ions greatly affect the ferrite overall properties. The wide variations in these properties arise from their ability to accommodate and distribute a variety of cations among the available tetrahedral (A) and octahedral (B) sites. Among those spinels is the magnesium–zinc ferrite chromate,  $Mg_{1-x}Zn_xFeCrO_4$ , which has many industrial applications [4]. The  $MgFeCrO_4$  is a magnetic material having a predominantly inverse structure, whereas the degree of inversion depends

\* Corresponding author.

E-mail address: [kadhimm@unizwa.edu.om](mailto:kadhimm@unizwa.edu.om) (K.A.M. Khalaf).

upon the method of preparation and heat treatment [5]. The zinc ferrite chromate,  $\text{ZnFeCrO}_4$  has the cation distribution of a completely normal spinel at room temperature. The  $\text{Zn}^{2+}$  and  $\text{Cr}^{3+}$  ions have strong preference to occupy the tetrahedral (A) and octahedral (B) sites respectively [6]. The lattice constants are related linearly to the ionic radii and the electro negativity of the constituting cations and anions. Simple empirical equations were used to predict efficiently the lattice constants in these spinels [7]. The spinel ferrites are characterized by showing four infrared absorbing bands, the first three bands were attributed to the intrinsic vibration of the metal oxygen complexes at the (A) and (B) sites, while the fourth band is attributed to some type of lattice vibrations [8].

The present paper reports on the compositional dependence of the structural and electrical properties of  $\text{Zn}^{2+}$  substituted Mg–ferrite chromate having the general chemical formula  $\text{Mg}_{1-x}\text{Zn}_x\text{FeCrO}_4$  ( $x = 0.0$  to  $1.0$  step  $0.2$ ), covering the entire range from  $\text{MgFeCrO}_4$  to  $\text{ZnFeCrO}_4$  spinels using the XRD, TEM, SEM, EDS, TGA, DTA, FT-IR and DC electrical resistivity tools at room temperature.

## 2. Experimental

Various compositions of the  $\text{Mg}_{1-x}\text{Zn}_x\text{FeCrO}_4$  ( $x = 0.0$ – $1.0$  step  $0.2$ ) spinels were synthesized using the conventional double sintering ceramic technique. High purity powders of  $\text{MgO}$ ,  $\text{ZnO}$ ,  $\text{Cr}_2\text{O}_3$  and  $\text{Fe}_2\text{O}_3$  oxides were weighed carefully to have the desired stoichiometric proportions and mixed in agate mortar. The mixture was first sintered at  $1000^\circ\text{C}$  for 24 h in air medium followed by slow cooling at room temperature. The powder then remixed and ground once more to promote homogeneity. Pellets of 13 mm in diameter and 2–3 mm thick were prepared using pressure of 10 tons/cm<sup>2</sup>. The pellets and powders were sintered at  $1100^\circ\text{C}$  for 24 h followed by natural cooling to room temperature. The X-ray diffraction spectrum of these samples were examined by Phillips PW1820 diffractometer with  $\text{CuK}\alpha$  radiation ( $\lambda = 1.5404\text{\AA}$ ). The scans range were kept the same for all samples ( $2\theta = 10^\circ$ – $100^\circ$ ) using a step size of  $0.02^\circ$  with sample time of 2s. Samples for recording IR spectra were prepared by mixing small quantity of the powder of the samples with solid KBr. The mixed powders of the samples were then pressed at 10 tons/cm<sup>2</sup> to produce thin cylindrical samples of 1.3 cm in diameter. The IR scans were recorded at room temperature in the range from 400 to  $1000\text{ cm}^{-1}$  using PERKIN-ELMER-1430 infrared spectrophotometer.

The microstructure and sample surface morphology were examined with analytical scanning electron microscope (ASEM) model JSM-6510LA-JEOL and transmission electron microscope model JEM-1400-JEOL. The energy dispersive spectroscopy (EDS) has been used to identify the sample constituent elements and their relative atomic and mass percentage. The DC resistance measurements at room temperature were performed by first grinding the surfaces of the cylindrical pellets to remove any oxide, such as  $\text{Fe}^{+2}$ , which might be caused by the distillation of the sample surface, such as the  $\text{Zn}^{+2}$ , during sintering at high temperature and to remove any contamination to the pellet surfaces during the pressing and heating process. The pellets surfaces were coated with silver paste conductor to ensure good electrical contact between the sample and the two copper terminals for the electrical resistance measurements. The TGA and DTA scans were recorded simultaneously using PerkinElmer STA6000 scanner in the temperature range  $30^\circ\text{C}$  to  $800^\circ\text{C}$  at  $5^\circ\text{C}/\text{min}$  in nitrogen atmosphere.

## 3. Results and discussion

The X-ray diffraction spectra of the various compositions of the

$\text{Mg}_{1-x}\text{Zn}_x\text{FeCrO}_4$  spinels are presented in Fig. 1. All the XRD-spectra showed reflections from the plains (111), (220), (311), (222), (400), (440), (422), (511), (620), (533). Careful examinations of the XRD spectra peaks reveal that they are not all purely single peaks. So it was decided to estimate the lattice constants using the detailed refinement approach. The outcomes of the refinement approach can be summarized in the following main points: First; The degree of inversion in the pure  $\text{MgFeCrO}_4$  ( $x = 0.0$ ) ferrite is only about 0.3. Second; The samples with  $x = 0.2, 0.4, 0.6$  are actually mixtures of pure  $\text{MgFeCrO}_4$  and Zn-doped  $\text{MgFeCrO}_4$ . So the values of  $x$  ( $=0.2, 0.4$  and  $0.6$ ) should only be taken in an average sense. What we have is a mixture of pure  $\text{MgFeCrO}_4$  and Zn-doped  $\text{MgFeCrO}_4$  compounds (the Zn contents in the later are different from the values of (0.2, 0.4 and 0.6). Third; for the samples with  $x = 0.8$  and  $1.0$ , the majority  $\text{Zn}^{2+}$  goes to the tetrahedral sites with a minority going to the octahedral sites. A refinement with  $\text{Zn}^{+2}$  cations only occupying the tetrahedral sites is less favorable than those given in Table 1. Results of the best Rietveld refinement of the X-ray powder diffraction data are shown in Fig. 2 and Table 1. Values of the average,  $a_{\text{exp}}$  are plotted in Fig. 3 as a function of  $\text{Zn}^{2+}$  ions contents. The  $a_{\text{exp}}$  values were found as  $8.361\text{ \AA}$  and  $8.382\text{ \AA}$  for the two end samples  $\text{MgFeCrO}_4$  and  $\text{ZnFeCrO}_4$  respectively. These values agree with reported results of  $8.39\text{ \AA}$  for  $\text{MgFeCrO}_4$  [9] and  $8.381\text{ \AA}$  for  $\text{Mg}_{0.5}\text{Zn}_{0.5}\text{FeCrO}_4$  [10]. The  $a_{\text{exp}}$  values for both phases increase with  $\text{Zn}^{+2}$  contents. The increase in the lattice parameters was attributed to the replacement of smaller  $\text{Fe}^{3+}$  ( $0.67\text{ \AA}$ ) ions with a larger ionic radius of the  $\text{Zn}^{2+}$  ( $0.74\text{ \AA}$ ). It is clear that values of  $a_{\text{exp}}$  support the refinement analysis and suggestions that the crystalline structure is a mixture of pure  $\text{MgFeCrO}_4$  (phase-I), which is predominately inverse spinel and Zn-doped  $\text{MgFeCrO}_4$  (phase-II), which is mixed inverse-normal spinel type structure. The magnesium ferrites chromate,  $\text{MgFeCrO}_4$  is a magnetic material having a mixture normal-inverse ferrites structure [5]. The zinc ferrite chromate,  $\text{ZnFeCrO}_4$  has the cation distribution of a completely normal spinel at room temperature [6]. Moreover, the  $\text{Zn}^{2+}$  and  $\text{Cr}^{3+}$  ions have strong preference to occupy the tetrahedral (A) and octahedral (B) sites, respectively. The refinement results for the cation distribution are shown in Table 1. Knowing the cation distributions allows the calculations of the average values of the ionic radii at the tetrahedral,  $r_A$  and octahedral sites,  $r_B$  using the following relations, which relates the ionic concentration and the ionic radius at the tetra- and octa-hedral sites [11].

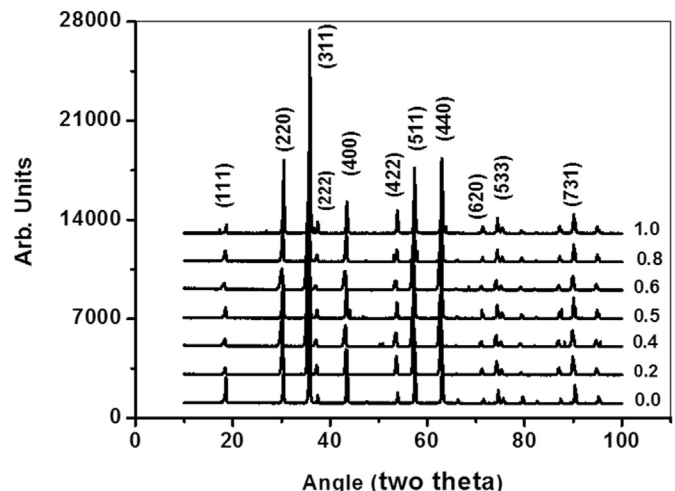


Fig. 1. The X-ray diffraction spectra for the  $\text{Mg}_{1-x}\text{Zn}_x\text{FeCrO}_4$  spinels.

**Table 1**  
The refinement results.

X	[A][B] <sub>2</sub> O <sub>4</sub>	a (Å)	Ions	Wyckoff site	x	y	z	Occupancy	R-factors				
0.0	[Mg <sub>0.52</sub> Fe <sub>0.48</sub> ] <sub>A</sub> [Mg <sub>0.48</sub> Fe <sub>0.52</sub> Cr <sub>1.0</sub> ] <sub>B</sub> O <sub>4</sub>	8.363	Mg <sup>+2</sup> (1)	8a	0.000	0.000	0.000	0.52	R <sub>w</sub> =13.6 R <sub>b</sub> =10.1 R <sub>exp</sub> =8.4				
			Mg <sup>+2</sup> (2)	16d	0.625	0.625	0.625	0.24					
			Fe <sup>+3</sup> (1)	8a	0.000	0.000	0.000	0.48					
			Fe <sup>+3</sup> (2)	16d	0.625	0.625	0.625	0.26					
			Cr <sup>+3</sup>	16d	0.625	0.625	0.625	0.5					
			O <sup>-2</sup> (1)	32e	0.383	0.383	0.383	0.93					
			O <sup>-2</sup> (2)	192i	-0.898	-0.355	0.071	0.01					
			0.2	[Mg <sub>0.16</sub> Fe <sub>0.84</sub> ] <sub>A</sub> [Mg <sub>0.84</sub> Fe <sub>0.16</sub> Cr] <sub>B</sub> O <sub>4</sub> (70%)	8.356	Mg <sup>+2</sup> (1)	8a	0.000		0.000	0.000	0.08	R <sub>w</sub> =13.8 R <sub>b</sub> =10.8 R <sub>exp</sub> =7.2
						Mg <sup>+2</sup> (2)	16d	0.625		0.625	0.625	0.21	
						Fe <sup>+3</sup> (1)	8a	0.000		0.000	0.000	0.42	
Fe <sup>+3</sup> (2)	16d	0.625				0.625	0.625	0.04					
Cr <sup>+3</sup>	16d	0.625				0.625	0.625	0.25					
O <sup>-2</sup> (1)	32e	0.388				0.388	0.388	0.37					
O <sup>-2</sup> (2)	192i	-0.317				0.523	-0.805	0.02					
0.4	[Mg <sub>0.75</sub> Fe <sub>0.25</sub> ] <sub>A</sub> [Mg <sub>0.25</sub> Fe <sub>0.75</sub> Cr] <sub>B</sub> O <sub>4</sub> (12%)	8.398				Mg <sup>+2</sup> (1)	8a	0.000	0.000	0.000	0.3	R <sub>w</sub> =10.8 R <sub>b</sub> =7.6 R <sub>exp</sub> =7.7	
						Mg <sup>+2</sup> (2)	16d	0.625	0.625	0.625	0.05		
						Fe <sup>+3</sup> (1)	8a	0.000	0.000	0.000	0.1		
			Fe <sup>+3</sup> (2)	16d	0.625	0.625	0.625	0.15					
			Cr <sup>+3</sup>	16d	0.625	0.625	0.625	0.2					
			O <sup>-2</sup> (1)	32e	0.388	0.388	0.388	0.15					
0.4	[Mg <sub>0.33</sub> Zn <sub>0.67</sub> ] <sub>A</sub> [FeCr] <sub>B</sub> O <sub>4</sub> (88%)	8.385	Mg <sup>+2</sup>	8a	0.000	0.000	0.000	0.2					
			Zn <sup>+2</sup>	8a	0.000	0.000	0.000	0.4					
			Fe <sup>+3</sup>	16d	0.625	0.625	0.625	0.3					
			Cr <sup>+3</sup>	16d	0.625	0.625	0.625	0.3					
			O <sup>-2</sup>	32e	0.384	0.384	0.384	0.6					
			O <sup>-2</sup> (2)	192i	-0.418	0.233	0.583	0.04					
0.6	[Mg <sub>0.4</sub> Fe <sub>0.6</sub> ] <sub>A</sub> [Mg <sub>0.6</sub> Fe <sub>0.4</sub> Cr] <sub>B</sub> O <sub>4</sub> (84%)	8.354	Mg <sup>+2</sup> (1)	8a	0.000	0.000	0.000	0.12	R <sub>w</sub> =14.9 R <sub>b</sub> =11.6 R <sub>exp</sub> =7.7				
			Mg <sup>+2</sup> (2)	16d	0.625	0.625	0.625	0.09					
			Fe <sup>+3</sup> (1)	8a	0.000	0.000	0.000	0.18					
			Fe <sup>+3</sup> (2)	16d	0.625	0.625	0.625	0.06					
			Cr <sup>+3</sup>	16d	0.625	0.625	0.625	0.15					
			O <sup>-2</sup> (1)	32e	0.381	0.381	0.381	0.24					
			O <sup>-2</sup> (2)	192i	-0.265	0.062	-0.435	0.01					
			0.6	[Mg <sub>0.14</sub> Zn <sub>0.86</sub> ] <sub>A</sub> [FeCr] <sub>B</sub> O <sub>4</sub> (16%)	8.406	Mg <sup>+2</sup>	8a	0.000		0.000	0.000	0.1	
						Zn <sup>+2</sup>	8a	0.000		0.000	0.000	0.6	
						Fe <sup>+3</sup>	16d	0.625		0.625	0.625	0.35	
Cr <sup>+3</sup>	16d	0.625				0.625	0.625	0.35					
O <sup>-2</sup>	32e	0.383				0.383	0.383	0.7					
O <sup>-2</sup> (2)	192i	0.196				-0.903	-0.348	0.003					
0.8	[Mg <sub>0.2</sub> Zn <sub>0.66</sub> Fe <sub>0.14</sub> ] <sub>A</sub> [Zn <sub>0.14</sub> Fe <sub>0.86</sub> Cr] <sub>B</sub> O <sub>4</sub>	8.374	Mg <sup>+2</sup>	8a	0.000	0.000	0.000	0.2	R <sub>w</sub> =13.2 R <sub>b</sub> =9.9 R <sub>exp</sub> =7.8				
			Zn <sup>+2</sup> (1)	8a	0.000	0.000	0.000	0.45					
			Zn <sup>+2</sup> (2)	16d	0.625	0.625	0.625	0.175					
			Fe <sup>+3</sup> (1)	8a	0.000	0.000	0.000	0.35					
			Fe <sup>+3</sup> (2)	16d	0.625	0.625	0.625	0.325					
			Cr <sup>+3</sup>	16d	0.625	0.625	0.625	0.5					
			O <sup>-2</sup> (1)	32e	0.385	0.385	0.385	0.98					
			O <sup>-2</sup> (2)	192i	0.196	-0.903	-0.348	0.003					
1.0	[Zn <sub>0.628</sub> Fe <sub>0.372</sub> ] <sub>A</sub> [Zn <sub>0.372</sub> Fe <sub>0.628</sub> Cr <sub>1.0</sub> ] <sub>B</sub> O <sub>4</sub>	8.382	Zn <sup>+2</sup> (1)	8a	0.000	0.000	0.000	0.628	R <sub>w</sub> =11.1 R <sub>b</sub> =7.6 R <sub>exp</sub> =7.4				
			Zn <sup>+2</sup> (2)	16d	0.625	0.625	0.625	0.186					
			Fe <sup>+3</sup> (1)	8a	0.000	0.000	0.000	0.372					
			Fe <sup>+3</sup> (2)	16d	0.625	0.625	0.625	0.314					
			Cr <sup>+3</sup>	16d	0.625	0.625	0.625	0.5					
			O <sup>-2</sup> (1)	32e	0.387	0.387	0.387	0.94					
			O <sup>-2</sup> (2)	192i	0.089	-0.777	0.085	0.019					

$$\left. \begin{aligned} r_A &= \sum_{i=0}^n C_n r_n \\ r_B &= \sum_{i=0}^n \frac{C_n r_n}{2} \end{aligned} \right\} \quad (1)$$

Where n, C<sub>n</sub> and r<sub>n</sub> are the number, concentration and radius of the ions at the A and B sites. C<sub>n</sub> values of the Mg<sup>2+</sup>, Zn<sup>2+</sup>, Fe<sup>3+</sup> and Cr<sup>3+</sup> ions have been taken from the refinement results Table 1. Values of the ion radius for Mg<sup>2+</sup> (0.66 Å), Zn<sup>2+</sup> (0.74 Å), Fe<sup>3+</sup> (0.67 Å) and Cr<sup>3+</sup> (0.63 Å) have been used in these calculations.

Values of the average values of the tetrahedral, r<sub>A</sub> and octahedral, r<sub>B</sub> ionic radii for each composition have been estimated and shown in Fig. 4 and Table 2. It is clear that values of r<sub>A</sub> and r<sub>B</sub> vary nonlinearly with Zn<sup>2+</sup> content. The variations of r<sub>A</sub> and r<sub>B</sub> reflect the changes of the cation distribution at the tetrahedral and octahedral sites, which can be explained as the increases in Zn<sup>2+</sup> concentration at the tetrahedral site cause the migration of an equivalent amount of the Fe<sup>3+</sup> ions from the tetrahedral site to the octahedral site to compensate for the reduction in the Mg<sup>2+</sup> ions at the octahedral site.

The overall resultant changes in the cation distribution were reflected in the increase of the lattice parameter a<sub>exp</sub> values with

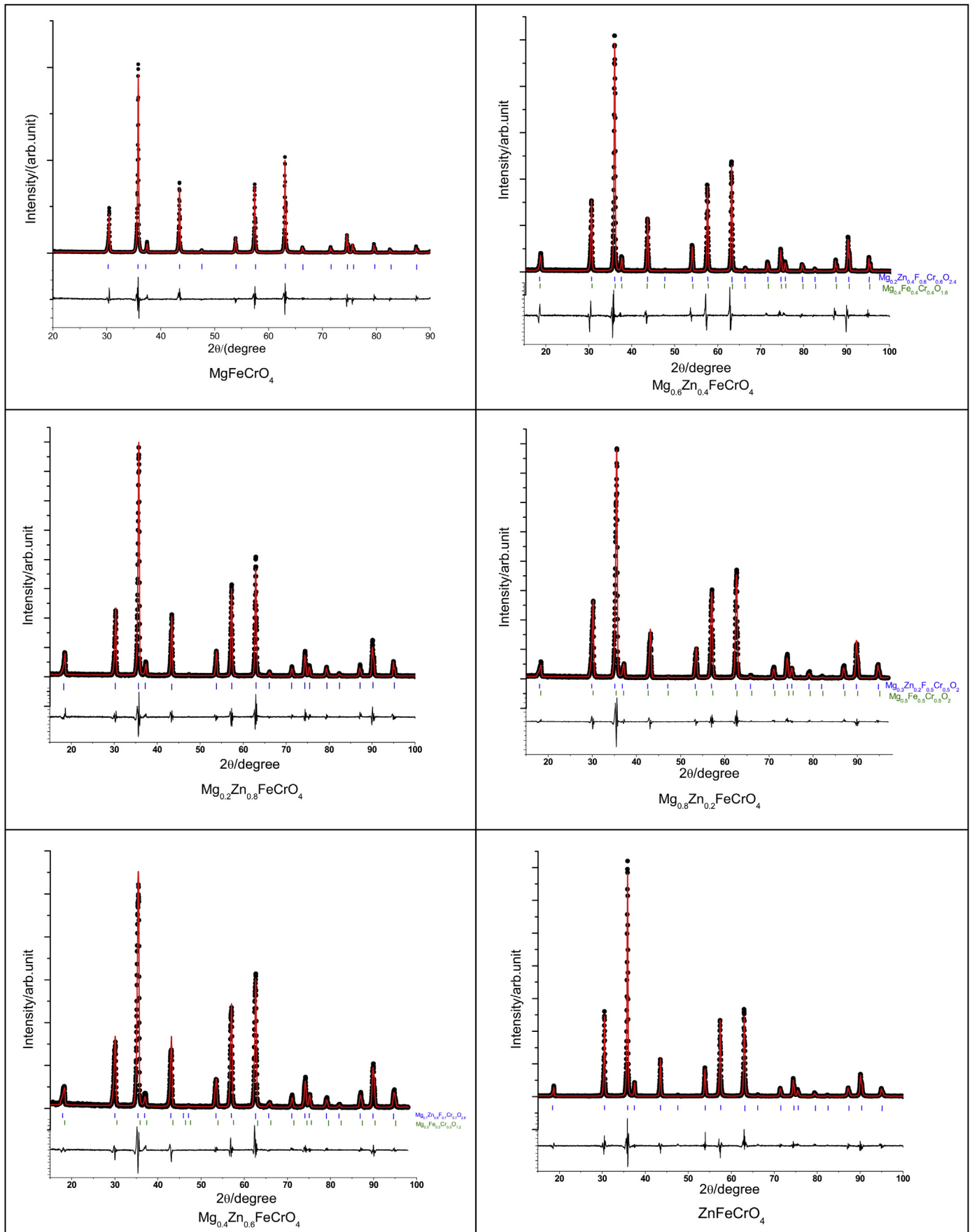


Fig. 2. The refinement of X-ray diffraction spectra for the  $\text{Mg}_{1-x}\text{Zn}_x\text{FeCrO}_4$  spinels.

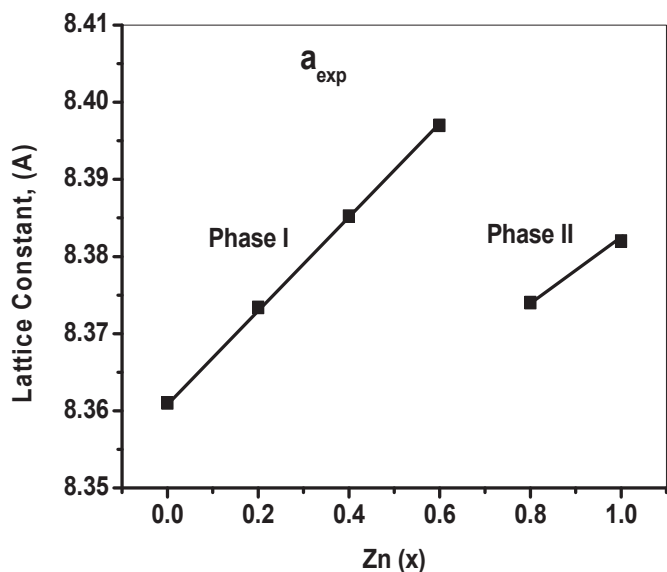


Fig. 3. The lattice constant,  $a_{exp}$  vs.  $Zn(x)$  for  $Mg_{1-x}Zn_xFeCrO_4$  spinels.

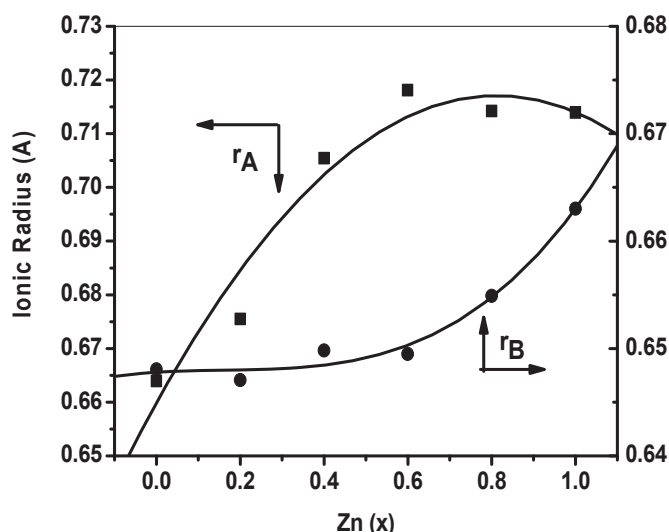


Fig. 4. The ionic radii  $r_A$  and  $r_B$  vs.  $Zn(x)$  for the  $Mg_{1-x}Zn_xFeCrO_4$  spinels.

Table 2  
Values of  $u$ ,  $r_A$ ,  $r_B$ ,  $a_{exp}$ ,  $a_{th1}$  and  $a_{th2}$  for the  $Mg_{1-x}Zn_xFeCrO_4$  spinels.

x	$u_{th}$	$u_{exp}$	$u_{avg}$	$r_A(\text{Å})$	$r_B(\text{Å})$	$a_{exp}(\text{Å})$	$a_{th1}(\text{Å})$	$a_{th2}(\text{Å})$
0.0	0.2560	0.2574	0.2568	0.6639	0.6480	8.3610	8.3661	8.3258
0.2	0.2568	0.2579	0.2572	0.6755	0.6471	8.3734	8.3792	8.3370
0.4	0.2576	0.2579	0.2577	0.7054	0.6498	8.3852	8.3910	8.3816
0.6	0.2584	0.2583	0.2581	0.7181	0.6495	8.3970	8.4034	8.3961
0.8	0.2592	0.2570	0.2585	0.7142	0.6549	8.3740	8.3785	8.4070
1.0	0.2600	0.2563	0.2589	0.7140	0.6630	8.3820	8.3856	8.4233
			Average			8.3788	8.3840	8.3785

$Zn^{2+}$  content. These results agree quite well with results for other ferrites chromate systems such as  $Cu_{1-x}Zn_xFeCrO_4$  [6],  $Ni_{1-x}Co_xFeCrO_4$  [12] and  $Ni_{1-x}Zn_xFeCrO_4$  [13].

It has been claimed [11] that a universal linear function exists between the lattice parameter,  $a_{exp}$  and the average ionic radii at the tetrahedral site,  $r_A$ . It is clear that the present results for the

$Mg_{1-x}Zn_xFeCrO_4$  spinels do not support this claim. A structural phase diagram can be constructed using the relation between the  $r_A$  and  $a_{exp}$  as shown in Fig. 5.

In order to calculate the theoretical values of the lattice constant “ $a_{th}$ ” and bond lengths at the tetrahedral, “ $R_A$ ” and octahedral, “ $R_B$ ” sites, the oxygen positional lattice parameter,  $u$ , has to be estimated. The ideal values of  $u$  can be taken for the perfect packing of ions within the lattice, as ( $u_{ideal}^A = 0.375$ ) where the origin at the tetrahedral site and ( $u_{ideal}^B = 0.250$ ) where the origin at the octahedral site. The relation between  $u^A$  and  $u^B$  can be written as ( $u^A = u^B + 0.125$ ). The value of  $u$  where the origin at B ( $u_{ideal} = 0.250$ ) is going to be used throughout this work. Accordingly the forms of the related equations are going to be chosen to fit these considerations. One way to estimate the average values of  $u(=u_1)$  for the  $Mg_{1-x}Zn_xFeCrO_4$  samples is by the interpolation between those reported earlier for pure magnesium,  $MgFe_2O_4$  and pure zinc,  $ZnFe_2O_4$  ferrites, which are equal to 0.256 and 0.260 respectively [14]. These values were assumed to hold true for  $MgFeCrO_4$  and  $ZnFeCrO_4$  because of the slender difference in the ionic radii of the  $Fe^{3+}$  and  $Cr^{3+}$  ions. Another method to estimate  $u$  values ( $=u_2$ ) is through the use of the following equation;

$$u = \frac{1}{2} - \frac{r_B + r_o}{a_{exp}} \quad (2)$$

Where  $r_B$  represents the mean ionic radius at the octahedral sites and  $r_o$  is the oxygen ion radius ( $=1.38 \text{ Å}$ ) [15]. Values of  $u$  from these two methods are shown in Table 2. It is clear that there is a good agreement between the two values. The difference between the two sets is less than ( $\pm 1\%$ ). Accordingly, the average values of  $u_{avg}$  have been found and employed in the calculation of the bond lengths  $R_A$  and  $R_B$ . It is clear that values of  $u_{avg}$  lie in the range (0.2568–0.2589) for the  $Mg_{1-x}Zn_xFeCrO_4$  spinels, in good agreement with those reported for large number of spinels (0.250–0.270) [16]. Moreover, these values satisfy the condition that has been imposed on the values of  $u$  for the formation of the spinel structure; which is ( $0.250 < u < 0.274$ ). The present values are not far from those reported for quite similar spinel such as  $MgFe_2O_4$  ( $u = 0.256$ ) and  $MgCr_2O_4$  ( $u = 0.2612$ ) [14,16]. Values of the  $u_{avg}$  increase with increasing the  $Zn^{2+}$  content. Similar results

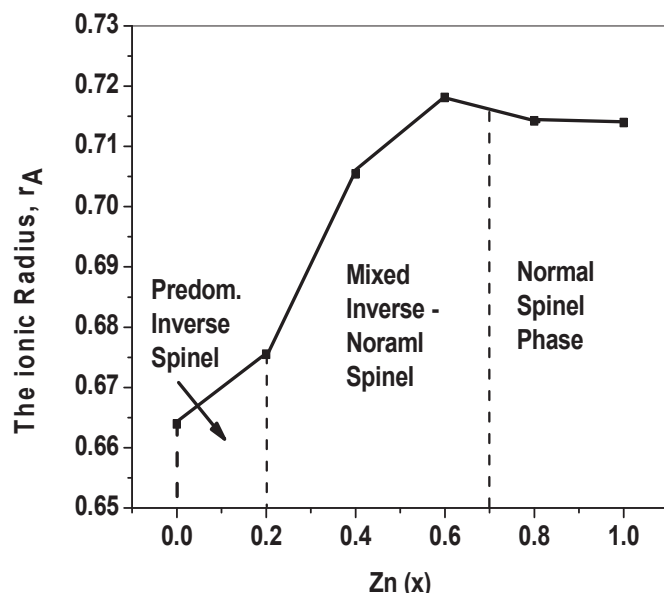


Fig. 5. The structural phase diagram for the  $Mg_{1-x}Zn_xFeCrO_4$  spinels.

have been reported for the  $\text{Ni}_{1-x}\text{Zn}_x\text{FeCrO}_4$  [14] and  $\text{Mg}_{1-x}\text{Zn}_x\text{Fe}_2\text{O}_4$  [17] ferrites. Like most spinel ferrites, the  $u$  values for the present series are higher than the ideal value ( $u = 0.250$ ), for which the anions are arranged in an ideal cubic closest-packing. This arises due to the adjustment of the lattice structure to accommodate the differences in the relative effective radii of cations at the tetrahedral and octahedral sites. As a result the oxygen ions will be displaced away (toward) from the nearest tetrahedral/octahedral cation in the [111] direction increasing (decreasing) the tetrahedron size and might be the octahedron size at the expense of each other [16].

The average bond lengths  $R_A$  and  $R_B$  at the tetrahedral and octahedral sites respectively can be evaluated using the relations [14–16];

$$\left. \begin{aligned} R_A &= a(u - 0.125)\sqrt{3} \\ R_B &= a\sqrt{3u^2 - 2u + 0.375} \end{aligned} \right\} \quad (3)$$

Values of  $R_A$  and  $R_B$  are shown in Table 3 and Fig. 6. It is clear that values of  $R_A$  increase first passing through broad maximum then decrease, while values of  $R_B$  increase slowly with increasing  $\text{Zn}^{2+}$  content. The bond lengths at tetrahedral sites,  $R_A$  is shorter than that at the octahedral sites,  $R_B$ . This might be caused by the migration of some  $\text{Zn}^{2+}$  cations from A-sites to B-sites, which leads to the expansion of the B-sites and to a relative displacement of the oxygen anions and causes shrinkage of the A-sites. This shrinkage has been correlated as more covalent bonding of cation–anion at the A-sites than that at the B-sites [18]. These results support the interpretation that correlates the decrease in the bond length to the increased covalent bonding characteristics such as the force constant between the cations and anions, which becomes greater. Similar results have been shown by other ferrite systems such as  $\text{Zn}_x\text{Cu}_{1-x}\text{FeCrO}_4$  [6] and  $\text{Mg}_{1-x}\text{Zn}_x\text{Fe}_2\text{O}_4$  [17]. The changes in  $R_A$  and  $R_B$  values with  $x$  might be controlled partially by variation in the cation distributions among the A- and B- sites during the substitution process.

Values of the differences in the Pauling electronegativities at the tetrahedral,  $\Delta\chi_A$  and octahedral,  $\Delta\chi_B$  sites can be estimated using the following relations [17,19];

$$\left. \begin{aligned} \Delta\chi_A &= \chi_o - \chi_A \\ \Delta\chi_A &= \Delta\chi_o - \sum_{i=0}^n \frac{C_n^A \chi_n^A}{4} \\ \Delta\chi_B &= \chi_o - \chi_B \\ \Delta\chi_B &= \chi_o - \sum_{i=0}^n \frac{C_n^B \chi_n^B}{12} \end{aligned} \right\} \quad (4)$$

where  $C_n^A$ ,  $C_n^B$ ,  $\chi_n^A$  and  $\chi_n^B$  are the cations concentration and Pauling electronegativity at the A- and B-sites. Values of the Pauling electronegativities are  $\chi_{\text{Mg}^{+2}} (=1.31)$ ,  $\chi_{\text{Zn}^{+2}} (=1.65)$ ,  $\chi_{\text{Fe}^{3+}} (=1.83)$ ,  $\chi_{\text{Cr}^{+2}} (1.66)$  and  $\chi_{\text{O}^{2-}} (=3.44)$  respectively. Values of  $\Delta\chi_A$  and  $\Delta\chi_B$  are shown in Table 4. The changes in values of the electronegativity

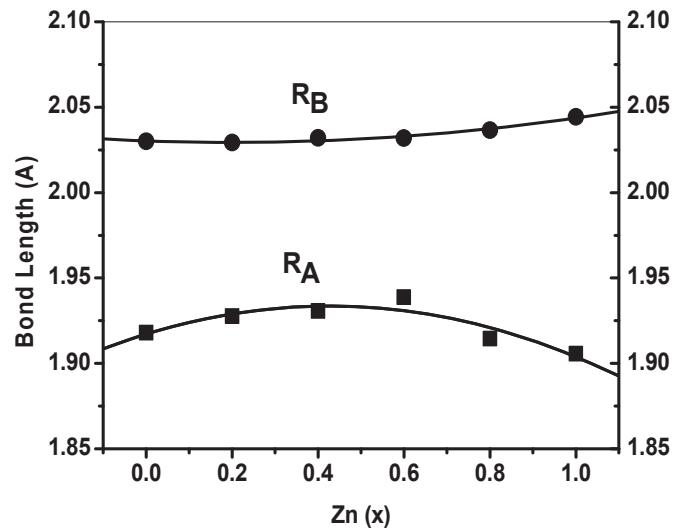


Fig. 6. The bond lengths  $R_A$  and  $R_B$  vs. Zn ( $x$ ) for  $\text{Mg}_{1-x}\text{Zn}_x\text{FeCrO}_4$  spinels.

differences reflect the bond length changes. These changes agree quite well with changes in values of the force constant  $K_t$  and  $K_o$  at the tetrahedral and octahedral sites respectively.

The theoretical values of the lattice parameter,  $a_{th}$  have been calculated using two different methods. In the first one the average bond lengths  $R_A$  and  $R_B$  at the tetrahedral and octahedral sites are related to  $a_{th1}$  as in the following equation [16]:

$$a_{th1} = \frac{8R_A}{3\sqrt{3}} + \frac{8R_B}{3} \quad (5)$$

the calculated values of  $a_{th1}$  are shown in Table 2. It is clear that values of “ $a_{th1}$ ” values are slightly higher than “ $a_{exp}$ ” values. In the second method a semi empirical linear formula has been employed, which relates the lattice constant,  $a_{th2}$  to the ionic radii ( $r_A$  and  $r_B$ ), the oxygen radius ( $r_O$ ) and their electronegativities ( $\chi_A$ ,  $\chi_B$  and  $\chi_O$ ) at the tetrahedral and octahedral sites. This equation has been used to calculate the lattice constants for large number of spinel oxides [7].

$$\begin{aligned} a_{th2} &= 1.27084(r_A + r_O) + 2.49867(r_B + r_O) + 0.0864(\chi_O - \chi_B) \\ &\quad + 0.05141(\chi_O - \chi_A) + 0.230 \end{aligned} \quad (6)$$

The calculated values of  $a_{th2}$  using this equation do not agree well with the present  $a_{exp}$  values. This equation has been slightly modified by adjusting the value of the constant term to be (0.230) instead of (0.6034). Results of the calculated lattice constants “ $a_{th2}$ ” are shown in Table 2. It is clear that the experimental and calculated values agree quite well with an average deviation of less than 1%.

Values of the crystallite size,  $D_{XRD}$  for each sample has been taken as the average of those calculated for the reflected peaks of

**Table 3**  
Values of  $R_A$ ,  $R_B$ ,  $D_{W-H}$ ,  $D_{XRD}$ ,  $d_{EXP}$ ,  $d_{XRD}$ ,  $2r$  and  $\epsilon$  as a function of Zn( $x$ ) for the  $\text{Mg}_{1-x}\text{Zn}_x\text{FeCrO}_4$  spinels.

X	$R_A$ (Å)	$R_B$ (Å)	$D_{W-H}$ (nm)	$D_{XRD}$ (nm)	$d_{EXP}$ (g/cm <sup>3</sup> )	$d_{XRD}$ (g/cm <sup>3</sup> )	$2r$ (cm)	$\epsilon \times 10^{-3}$ (W-H equation)
0.0	1.9180	2.0299	10.8	28.7	3.2938	4.4608	1.200	3.686
0.2	1.9277	2.0292	8.6	21.9	3.5053	4.6513	1.195	4.955
0.4	1.9307	2.0320	8.3	23.6	3.1492	4.8213	1.245	4.660
0.6	1.9388	2.0319	7.6	20.6	3.4319	4.9970	1.222	5.142
0.8	1.9145	2.0366	8.0	20.1	3.6213	5.1784	1.220	5.187
1.0	1.9057	2.0444	9.8	24.3	3.6434	5.3623	1.248	4.309

**Table 4**  
Values of  $v_1$ ,  $v_2$ ,  $K_t$ ,  $K_o$ ,  $\Delta\chi_A$  and  $\Delta\chi_B$  as a function of Zn(x) for the  $Mg_{1-x}Zn_xFeCrO_4$  spinels.

x	$v_1$ (cm <sup>-1</sup> )	$v_2$ (cm <sup>-1</sup> )	$K_t \times 10^5$ (dyne/cm)	$K_o \times 10^5$ (dyne/cm)	$\Delta\chi_A$	$\Delta\chi_B$
0.0	625	497	1.0915	1.2523	3.0615	3.1662
0.2	621	496	1.4040	1.1665	3.0259	3.1747
0.4	614	494	1.3987	1.3811	3.0595	3.1509
0.6	612	494	1.3134	1.1939	3.0388	3.1536
0.8	606	492	1.5625	1.4033	3.0382	3.1818
1.0	602	491	1.7077	1.4260	3.0108	3.1548

the (hkl) planes for the concerned sample using Debye-Scherrer's equation [15];

$$D_{hkl} = \frac{K\lambda}{\beta_{hkl} \cos\theta_{hkl}} \quad (7)$$

Where K is constant (=0.9) and  $\beta_{hkl}$  is the width at half maximum of the reflected peak of the (hkl) plane at the reflected angle  $\theta_{hkl}$  and  $\lambda$  (=1.5404 Å) is the x-ray wavelength. The average value of the X-ray density,  $D_{XRD}$ , for each sample has been found by taking the average of the  $D_{hkl}$  values for the concerned sample.  $D_{XRD}$  values are shown in Table 3 and the inset in Fig. 7. The average value of these values was estimated to be (22 ± 7) nm. Moreover, the average crystallite size  $D_{W-H}$  can be estimated for each sample using the Williamson–Hall plot [20];

$$\beta_{hkl} \cos\theta_{hkl} = \frac{0.9\lambda}{D_{W-H}} + 4\epsilon \sin\theta_{hkl} \quad (8)$$

The average particle size,  $D_{W-H}$  and the micro-strain introduced inside the sample,  $\epsilon$ , can be estimated from the intercept and slope of the fitted straight line between values of ( $\beta_{hkl}\cos\theta_{hkl}$ ) and ( $4\epsilon\sin\theta_{hkl}$ ) for each sample respectively. Values of  $D_{W-H}$  are shown in Table 3. Fig. 7 shows values of  $D_{W-H}$  as a function of Zn<sup>+2</sup> content. The average value for  $D_{W-H}$  was found to be (9 ± 2) nm. Similar results have been reported for the  $NiFe_{2-x}Cr_xO_4$  [21] and  $MgFe_{2-x}Cr_xO_4$  [9] spinels. Values of  $D_{XRD}$  and  $D_{W-H}$  decrease first, pass through minimum then increase with Zn<sup>+2</sup> content. Values of both  $D_{XRD}$  and  $D_{W-H}$  are much smaller than those obtained from SEM scans. This might be caused by the secondary particles effects on the SEM scans. The average sizes of grain crystallites obtained from the SEM micrographs agree with those obtained from refinement analysis. Values of  $\epsilon$  increase first passing through a

maximum centered at about x = 0.6 then it decrease as shown in Fig. 8. The general trend of data variation of  $\epsilon$  supports the variation trends in the crystallite sizes, volume expansion and porosity. Similar results have been reported for the effects of Zn<sup>2+</sup> ions on the micro-strain inside the samples of  $Zn_{1-x}Cd_xFe_2O_4$  [22] and  $Mg_{1-x}Zn_xFe_2O_4$  [17] ferrites.

The bulk (experimental) density,  $d_{exp}$  ( $=m/(\omega\pi r^2)$ ), X-ray (true) density,  $d_{XRD}$  ( $=ZM/VN_A$ ) and porosity,  $p$  ( $=(d_{XRD}-d_{exp})/d_{XRD}$ ) where m,  $\omega$ , r, and V represent the mass, thickness, radius and volume of the pellet respectively, while Z, M and  $N_A$  represent the number of molecules per unit cell (=8), average molecular weight and Avogadro's number respectively. Values of the calculated  $d_{XRD}$  and  $d_{exp}$  are shown in Table 3 and plotted in Fig. 9 as a function of Zn<sup>+2</sup> content in the sample. Both  $d_{exp}$  and  $d_{XRD}$  densities increase with increasing Zn<sup>+2</sup> content. This might be caused by the replacement of Mg (23.985 g/mole) with a more massive element, Zn (65.926 g/mole). The true density,  $d_{XRD}$ , is higher than the bulk density,  $d_{exp}$ , for all samples. The  $d_{exp}$  values form 65–67% of  $d_{XRD}$ . The difference between values of  $d_{exp}$  and  $d_{XRD}$  might be attributed to the creation of pores in the samples during the sintering processes at high temperatures. The apparent porosity and the volume expansion in these samples increase with increasing Zn<sup>+2</sup> content as shown in Figs. 8 and 9. Similar porosity, density and grain size results have been reported for the  $Mg_{1-x}Zn_xFe_2O_4$  [17] and  $NiFe_{2-x}Cr_xO_4$  [21] ferrites.

The thermo-gravimetric and differential thermal analyses were performed using STA 6000-Perkin Elmer at heating rate 5 °C/min in temperature range from 30 °C to 800 °C under N<sub>2</sub> atmosphere with flow rate of 30 mL/min. The results of the TGA and DTA scans for samples with (z = 0.0, 0.4, 0.6 and 1.0) are shown in Fig. 10. The TGA

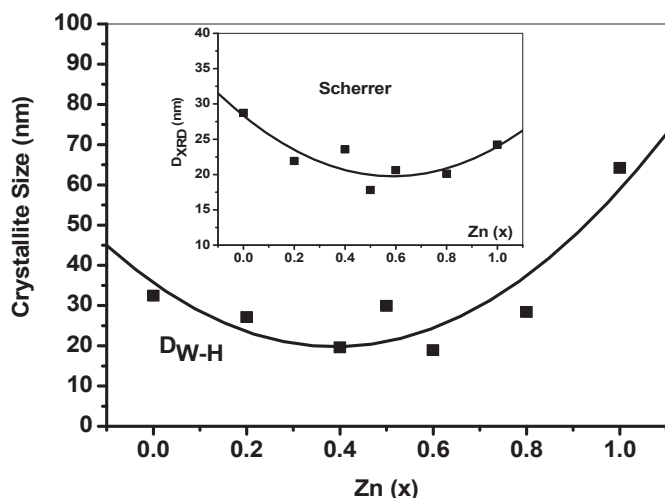


**Fig. 7.** The crystallite sizes  $D_{W-H}$  and  $D_{XRD}$  vs. Zn(x) for the  $Mg_{1-x}Zn_xFeCrO_4$  spinels.

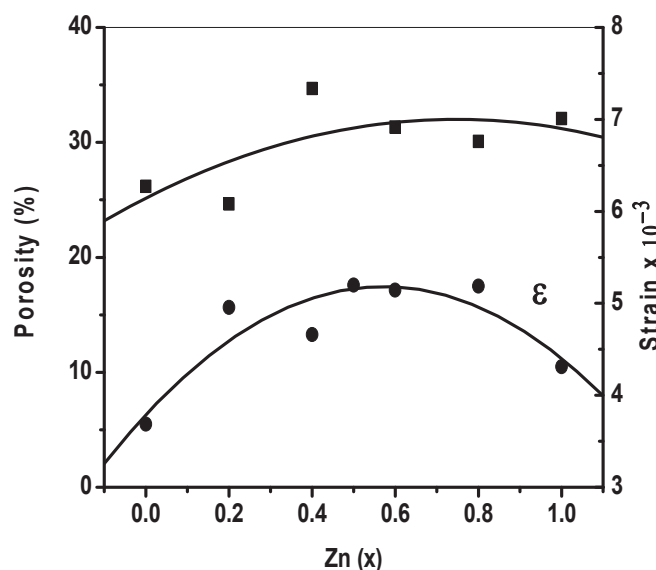


**Fig. 8.** The porosity and micro-strain vs. Zn(x) for the  $Mg_{1-x}Zn_xFeCrO_4$  spinels.

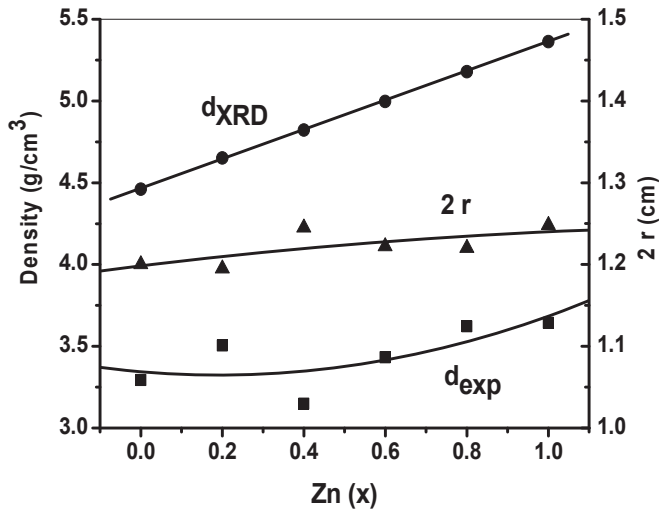


Fig. 9. The densities  $d_{\text{XRD}}$ ,  $d_{\text{exp}}$  and sample diameter,  $2r$  for the  $\text{Mg}_{1-x}\text{Zn}_x\text{FeCrO}_4$  spinels.

curve analysis shows that there is mass loss with temperature. The loss of mass might be caused by vaporization of surface water molecules at first followed by vaporization of the trapped water molecules at higher temperatures. The DTA analysis showed no

abrupt changes and no sharp endo-/exo-thermic peaks have been recorded, which indicates the ferrite formation has been completed during heat treatment process of the sample preparation.

The sample surface morphologies mapping of the  $\text{Mg}^{2+}$ ,  $\text{Zn}^{2+}$ ,  $\text{Fe}^{3+}$  and  $\text{Cr}^{3+}$  ions in the  $\text{Mg}_{1-x}\text{Zn}_x\text{FeCrO}_4$  spinels are shown in Fig. 11. It is clear that the constituent cations are uniformly distributed throughout the sample surfaces.

The results of the analytical scanning confirm the purity of these samples and the lack of any considerable quantities of impurities. The chemical compositions of the  $\text{Mg}_{1-x}\text{Zn}_x\text{FeCrO}_4$  samples have been determined using the energy dispersive X-ray (EDS) spectroscopy. A representative energy dispersive spectrum of the samples with  $x = 0.4$  and  $0.8$  are shown in Fig. 12a and b. The elemental analysis of the EDS spectrums are in good agreement with the expected ratio of the starting raw oxides. The EDS spectrums of the samples with  $x = 0.4$  and  $0.8$  composed of Mg, Zn, Fe, Cr and O elements. The tables attached to Fig. 12a and b shows the atomic and mass percentages of the  $\text{Mg}^{2+}$ ,  $\text{Zn}^{2+}$ ,  $\text{Fe}^{3+}$ ,  $\text{Cr}^{3+}$  and  $\text{O}^{2-}$  ions in the samples with ( $x = 0.4$ ) and ( $x = 0.8$ ) respectively. It is clear that the EDS average mole ratios of these elements are in good agreement (within the experimental errors) with the expected nominal values. Accordingly, the sample compositions were taken to be equal to the nominal compositions.

The scanning electron microscope (SEM) and the transmission electron microscope (TEM) images show that the sample surfaces composed of a well-packed and continuous grain structure with

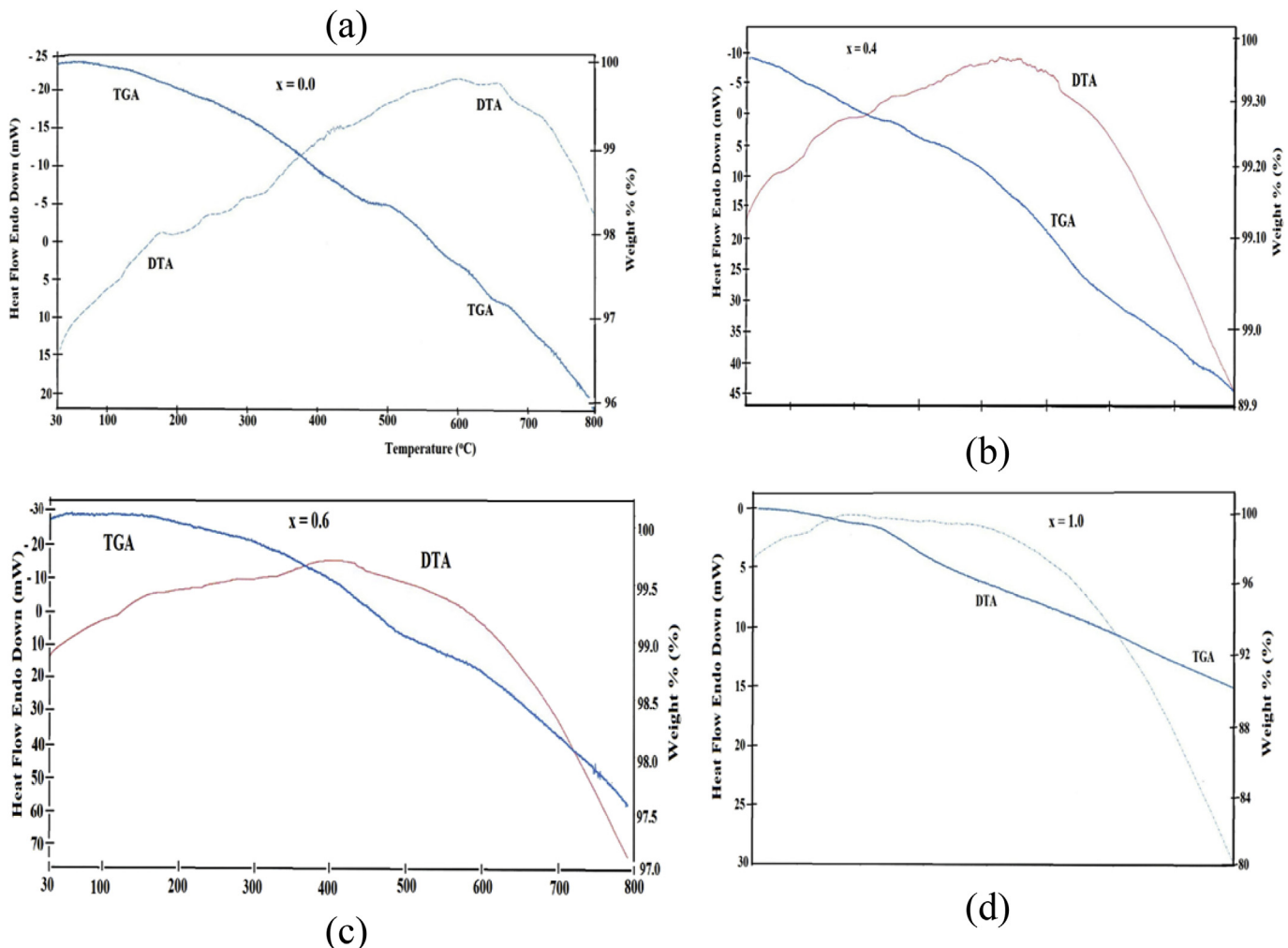


Fig. 10. The TGA and DTA scans for  $x = 0.0$  (a),  $x = 0.4$  (b),  $x = 0.6$  (c) and  $x = 1.0$  (d) in the  $\text{Mg}_{1-x}\text{Zn}_x\text{FeCrO}_4$  spinels.

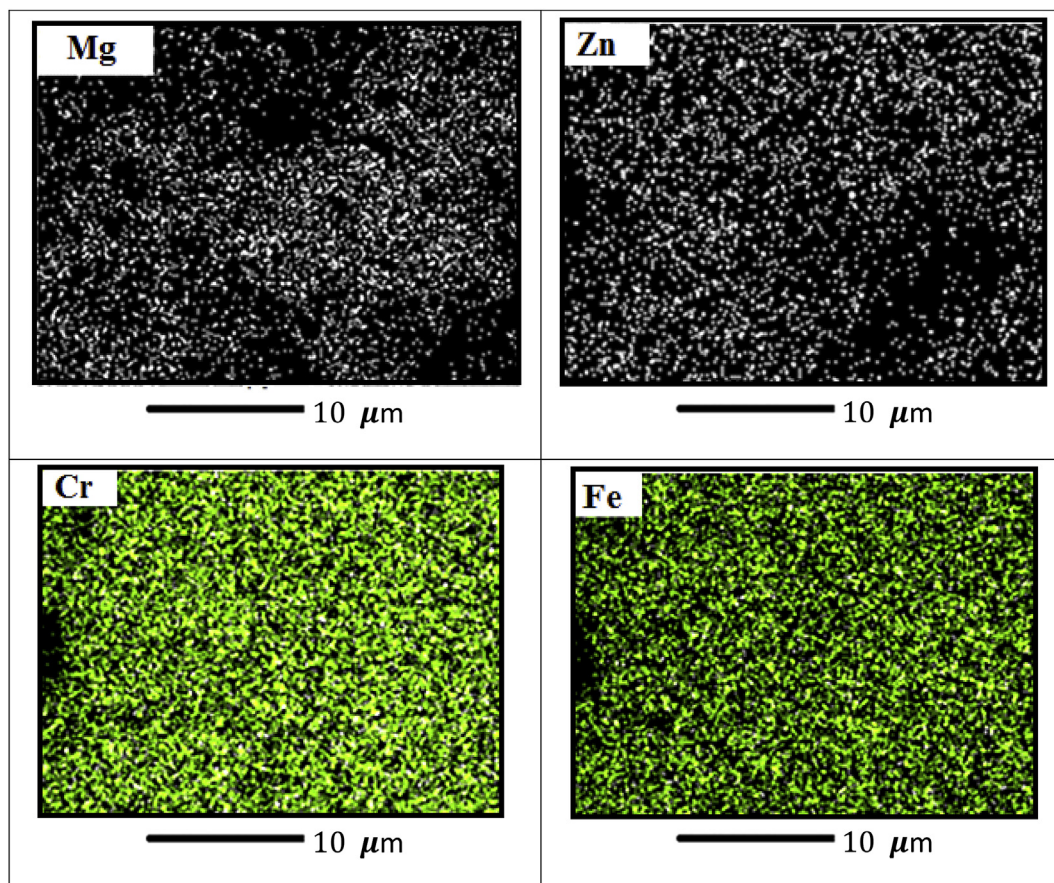


Fig. 11. Mapping of the cations distributions on the sample surface for the  $Mg_{1-x}Zn_xFeCrO_4$  spinels.

porosity and small holes at the grains boundaries of approximately cubic/spherical grains. It also shows the presence of large agglomeration phenomenon in the grains, which might be caused by the high temperature treatments. The average crystallite sizes were also determined using the X-ray diffraction data. Values of the crystallite sizes differ significantly from those determined from SEM scans. This is might be explained as the SEM micrographs give the size of the secondary particles, and the X-ray line broadening analysis discloses only the size of primary particles. The SEM and TEM micrographs of the  $Mg_{1-x}Zn_xFeCrO_4$  spinels are shown in Fig. 13 and Fig. 14 respectively. The SEM micrographs clearly show aggregates of well-defined cubic to spherical shapes of stacked grains of about (200 nm–1  $\mu$ m), which might be caused by the annealing at high temperatures (>1000  $^{\circ}$ C) for long time (24 h). Similar grain sizes have been reported for the Mg–Zn ferrites system [17,23]. Values for the grain crystallites sizes obtained from SEM and TEM micrographs are larger than those obtained from the XRD scans using Scherrer's equation and Williamson–Hall plot.

The DC-electrical resistivities for the  $Mg_{1-x}Zn_xFeCrO_4$  spinels at room temperature are shown in Table 5 and Fig. 15 (the inset shows  $\log(\rho)$  vs.  $Zn(x)$ ). All samples showed high resistivity of order ( $10^8$ – $10^{10}$ )  $\Omega$ -cm. Similar results have been reported for the  $Mg_{0.5}Zn_{0.5}Fe_{2-x}Cr_xO_4$  [24] and  $Co_{0.6}Zn_{0.4}Fe_{2-x}Cr_xO_4$  [25] spinels. It is clear that the resistivity of these spinels decreases with increase in  $Zn^{+2}$  content. The addition of larger ionic sized  $Zn^{2+}$  ions distorts the ferrite lattice by increasing the lattice parameter, " $a_{exp}$ ". It is well known that the  $Mg^{+2}$  and  $Cr^{+3}$  ions have strong tendency to occupy the octahedral B-sites, while the  $Zn^{+2}$  ions prefer to occupy the tetrahedral A-sites. As  $Zn^{+2}$  content increases at the A-sites, the

$Mg^{+2}$  ions concentration at the B-sites will decrease. As a result some of the  $Fe^{+3}$  ions will be forced to move from A-sites to B-sites to compensate for the reduction in  $Mg^{2+}$  concentration at this site. This lead to the increase in the hopping processes for both electrons and holes and to reduce the indirect interaction between the  $Fe^{+3}$  ions on the A- and B-sites. The motion of charges will be affected by this distortion causing the resistivity of these samples to decrease (increase in conductivity) as the  $Zn^{2+}$  content increases. The increase of  $Zn^{+2}$  ions enhances the electrical conduction mechanism. Careful analysis of the results in Figs. 5 and 15 and the inset in Fig. 15 show that there are three distinct regions, which might suggest that there are three different crystalline structures belong to three composition ranges; the first range ( $0.0 \leq x \leq 0.2$ ) are predominantly inverse spinels, the second range ( $0.2 < x < 0.8$ ) are mixture of inverse-normal spinel phase and the third range ( $x \geq 0.8$ ) are normal spinel phase. The distinct compositions between the three regions are around ( $x = 0.2$ ) and ( $x = 0.8$ ). Many Zn-ferrites show significant behaviors at low content of  $Zn^{+2}$  ions, among those is the improvements of the magnetic properties of the  $Co_{1-x}Zn_xFe_2O_4$  ferrites [26]. The improvement might be caused by the gradual phase structural changes from the inverse to normal spinel structures.

The relation between the electrical resistivity and porosity is shown in Fig. 16. It is clear that the resistivity decreases with increasing the porosity factor. Such behavior might be caused by the existence of loosely trapped, opened and randomly distributed pores with entrapped impurities inside those pores throughout the pellets, which provide easy electrical conduction paths. Similar results have been reported for other ferrite systems [27,28].

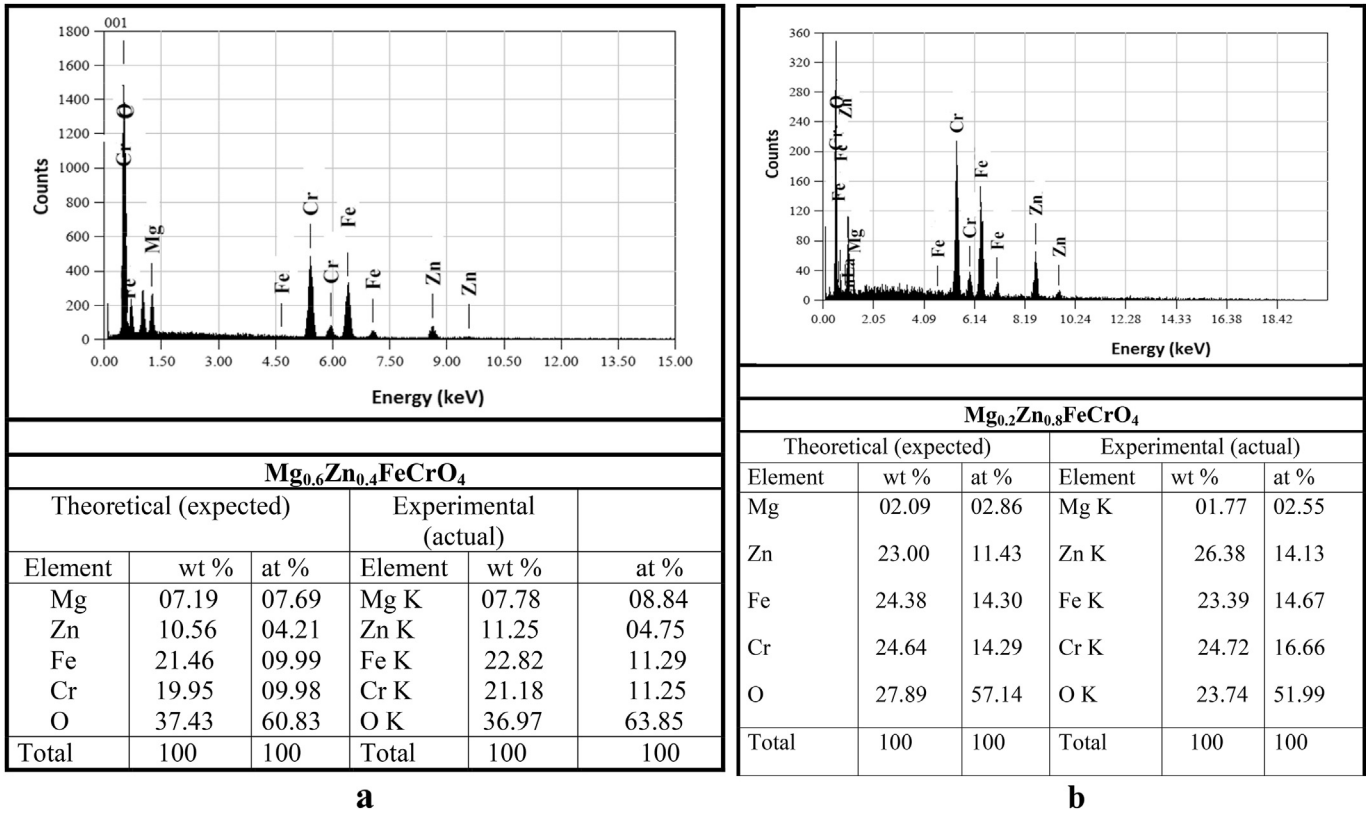


Fig. 12. a. The EDS analysis results for the sample with  $x = 0.4$  in the  $Mg_{1-x}Zn_xFeCrO_4$  spinels. b. The EDS analysis results for the sample with  $x = 0.8$  in the  $Mg_{1-x}Zn_xFeCrO_4$  spinels.

The FT-IR transmission spectra of the  $Mg_{1-x}Zn_xFeCrO_4$  spinels in the range  $400\text{--}1000\text{ cm}^{-1}$  are shown in Fig. 17. The IR spectra show two dominant absorption bands  $\nu_1$  and  $\nu_2$ . The band positions  $\nu_1$  and  $\nu_2$  are listed in Table 4 as a function of  $Zn^{+2}$  content. These

bands are common features of all the spinel ferrites [8]. Values of  $\nu_1$  and  $\nu_2$  values lie in the range  $(602\text{--}625\text{ cm}^{-1})$  and  $(491\text{--}497\text{ cm}^{-1})$  respectively. The wave numbers of the two bands  $\nu_1$  and  $\nu_2$  decrease with increasing  $Zn^{2+}$  ions in the sample as shown in

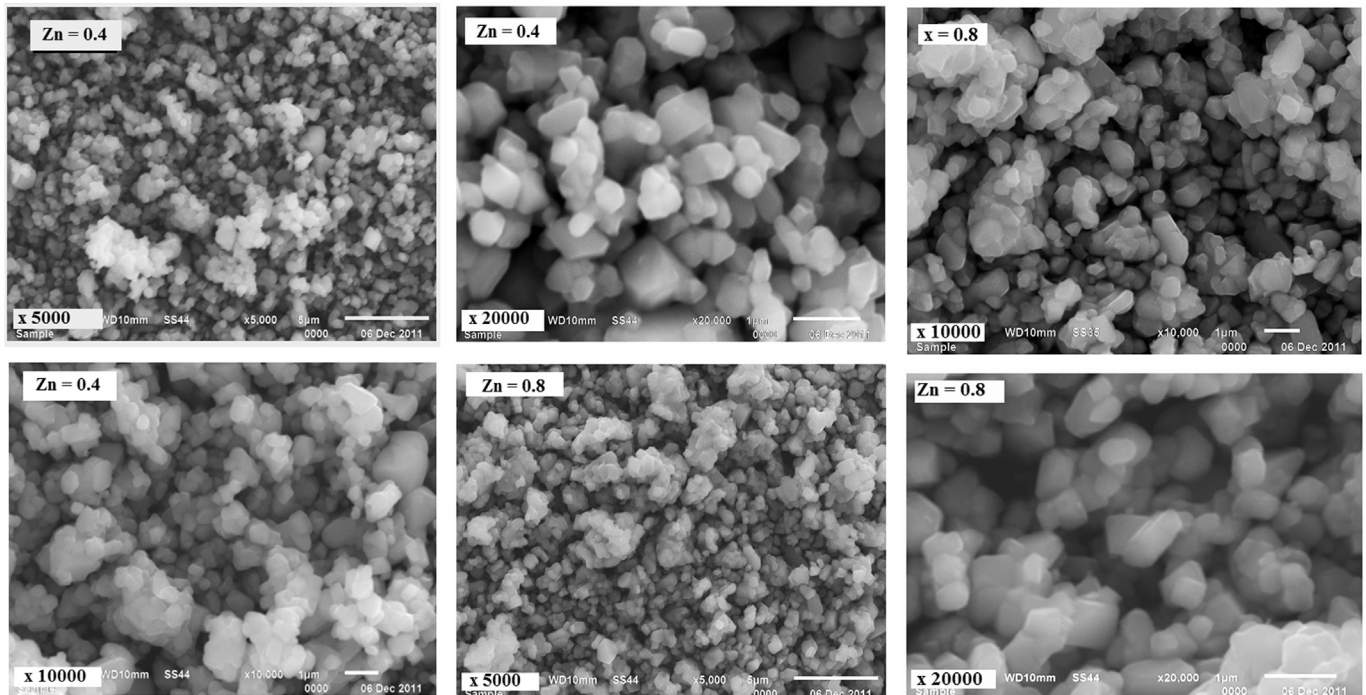


Fig. 13. The SEM images for the samples with  $x = 0.4$  and  $0.8$  at different magnification powers for the  $Mg_{1-x}Zn_xFeCrO_4$  spinels.

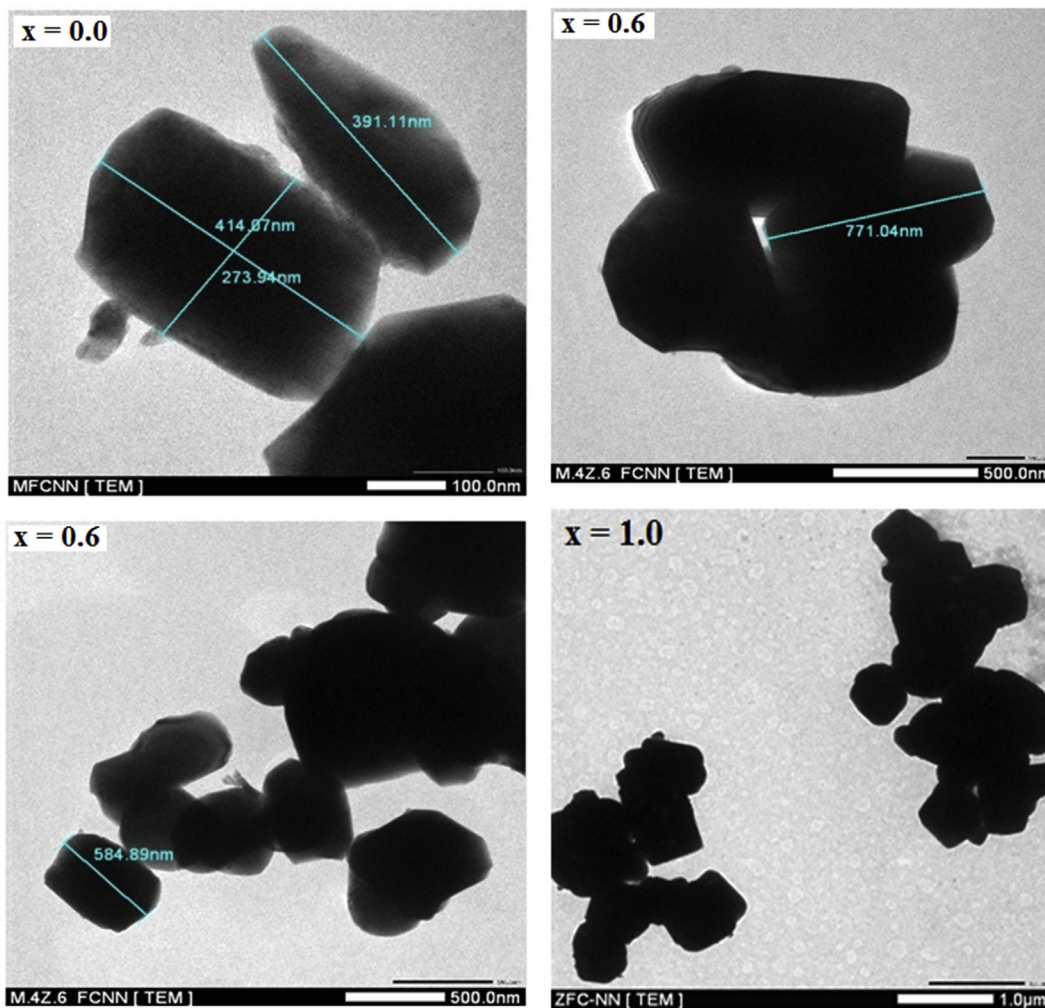


Fig. 14. The TEM images for the samples with  $x = 0.0, 0.6$  and  $1.0$  for the  $Mg_{1-x}Zn_xFeCrO_4$  spinels.

Table 5  
Values of  $\rho$ ,  $P_A$ ,  $P_B$ ,  $\alpha$  and  $\beta$  as a function of  $Zn(x)$  for the  $Mg_{1-x}Zn_xFeCrO_4$  spinels.

$x$	$\rho 10^{-9} (\Omega\text{-cm})$	$P_A$	$P_B$	$\alpha$	$\beta$
0.0	4.8036	0.8103	1.0029	0.6504	0.1823
0.2	0.1555	0.8108	1.0033	0.6482	0.2067
0.4	0.1905	0.7806	1.0034	0.6483	0.2075
0.6	0.3665	0.7782	1.0037	0.6466	0.2280
0.8	0.2315	0.7484	1.0026	0.6524	0.1610
1.0	1.4724	0.7363	1.0020	0.6517	0.1285

Fig. 18. The first band frequency  $\nu_1$  at the tetrahedral site is higher than that at the octahedral site  $\nu_2$ . This might be related to changes in the ionic radii at the A- and B- sites respectively. The high-frequency band  $\nu_1$  arises due to the stretching vibration of the tetrahedral metal–oxygen bonds and the low frequency band  $\nu_2$  is due to the metal–oxygen vibrations at the octahedral sites. The difference in the position of the two bands can be related to the changes in the cation distribution and to the differences in the average metal–oxygen distances and the electronegativities at the A- and B-sites. It is clear that the average bond length at tetrahedral sites,  $R_A$ , is shorter than that at the octahedral sites,  $R_B$ . This variation in the band position can be related to some extent to the variations in the average ionic radii at the A- and B- sites. These results agree with results of the  $Mg_{1-x}Zn_xFe_2O_4$  [17],  $Cu_{1-x}Zn_xFeCrO_4$  [6] and

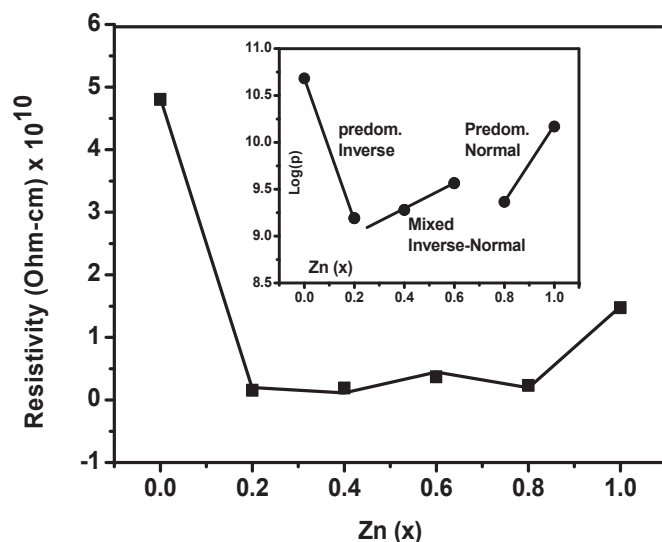


Fig. 15. The DC electrical resistivity,  $\rho$  vs.  $Zn(x)$  for the  $Mg_{1-x}Zn_xFeCrO_4$  spinels. The inset is  $(\log \rho$  vs.  $Zn(x))$ .

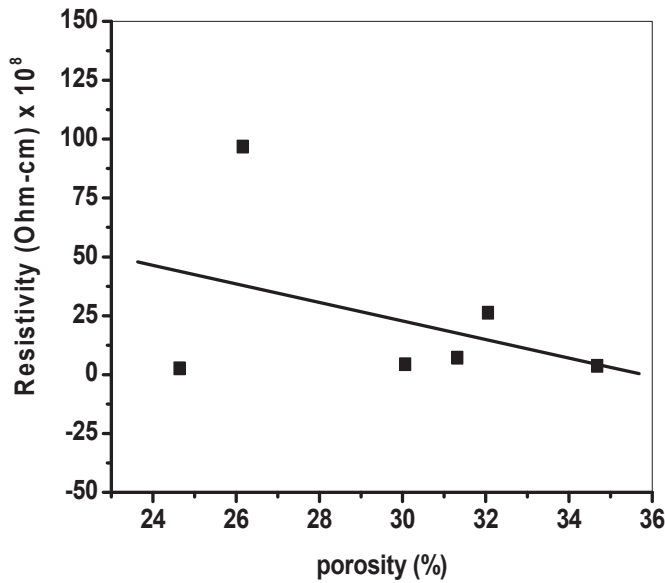


Fig. 16. The DC electrical resistivity,  $\rho$  vs. Porosity for the  $Mg_{1-x}Zn_xFeCrO_4$  spinels.

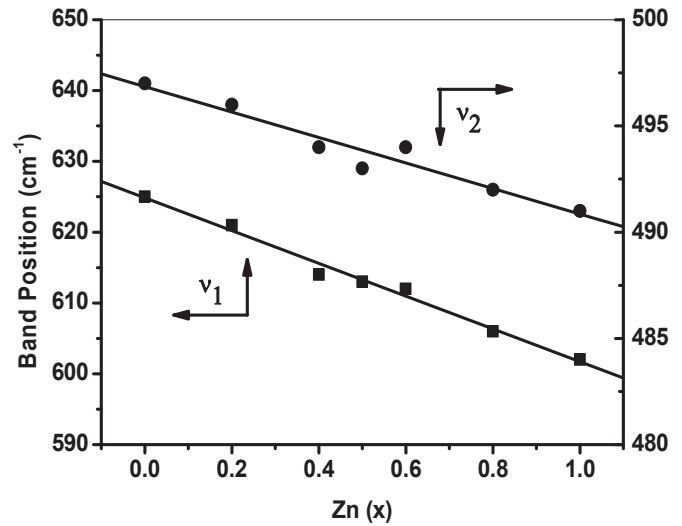


Fig. 18. The IR absorption bands  $\nu_1$  and  $\nu_2$  vs.  $Zn(x)$  for the  $Mg_{1-x}Zn_xFeCrO_4$  spinels.

transfers to the normal spinel phase,  $ZnFeCrO_4$ . Similar results have been shown by the  $Zn_{1-x}Ni_xFe_2O_4$  ferrites [30].

The force constants at the tetrahedral site,  $K_t$  and octahedral site,  $K_o$  have been calculated by substituting the IR band frequencies  $\nu_1$  and  $\nu_2$  in the following standard formulae [8];

$$\left. \begin{aligned} K_t &= 7.62M_1\nu_1^2 10^{-3} \left( \frac{\text{dyne}}{\text{cm}} \right) \\ K_o &= 10.62 \left( \frac{M_2}{2} \right) \nu_2^2 10^{-3} \left( \frac{\text{dyne}}{\text{cm}} \right) \end{aligned} \right\} \quad (9)$$

Where  $M_1$  and  $M_2$  are the average molecular mass of the cations at the tetrahedral and octahedral sites respectively, which have been calculated using the cation distributions. Values of  $K_t$  and  $K_o$  are shown in Table 4. It is clear that values of  $K_t$  are higher than those for  $K_o$ . This behavior might be caused by the difference in band stretching at the A- and B- sites. Values of the force constants at the tetrahedral and octahedral sites are influenced by many factors such as the strength of stretching, cation–oxygen bond length, the average molecular mass and electronegativity at these sites. Accordingly, the higher band stretching at the tetrahedral sites might be the cause of the higher force constant than that at the octahedral sites [8]. It is clear that the total number of  $Zn^{2+}$  ions at A-sites and  $Fe^{3+}$  ions at B-sites increase by increasing the  $Zn^{2+}$  content, which results in the cation redistributions at the A- and B-sites and the charge imbalance at the A- and B-sites, which is likely to shift the oxygen ions towards the  $Zn^{2+}$  ions at the A-sites and  $Fe^{3+}$  and  $Cr^{3+}$  ions at the B-sites making the force constant to increase at the A- and B- sites as  $x$  increases. The increases in the values of the force constant,  $K_t$  and  $K_o$  and electronegativities at the tetrahedral and octahedral sites justify the variations in values of the tetrahedral and octahedral bond lengths at these sites. Values of the force constants  $K_t$  and  $K_o$  have been plotted against the bond lengths  $R_A$  and  $R_B$  in Fig. 19. Variations of the force constants and the electronegativity differences values at the tetrahedral,  $\Delta\chi_A$  and octahedral,  $\Delta\chi_B$  sites support such explanations. Similar results have been reported for the  $Mg_{1-x}Zn_xFe_2O_4$  [17] ferrites. The changes in the cation distributions are usually reflected on the bandwidths of the IR spectra bands. Accordingly, the ratio of the half bandwidth maximum (HWMF) values of  $\nu_1$  and  $\nu_2$  at the A- and B- sites are calculated and presented in Fig. 20. It is clear that the ratio increases smoothly with the increase in the  $Zn^{2+}$  content in the sample.

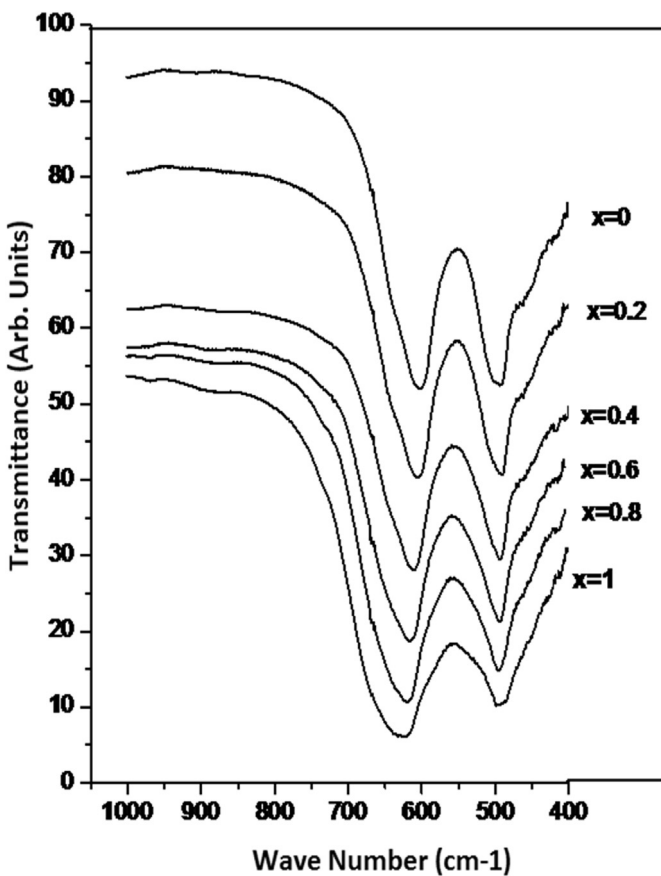


Fig. 17. Infrared spectra  $\nu_1$  and  $\nu_2$  vs.  $Zn(x)$  for the  $Mg_{1-x}Zn_xFeCrO_4$  spinels.

$ZnCr_{2-x}Fe_xO_4$  [29] spinels. It is expected that the transfer from the inverse spinel phase to the normal spinel phase in ferrites will be accompanied by decreasing in the stretching frequencies. This is supported by the present results, in which the frequencies  $\nu_1$  and  $\nu_2$  decrease as the predominately inverse spinel phase,  $MgFeCrO_4$

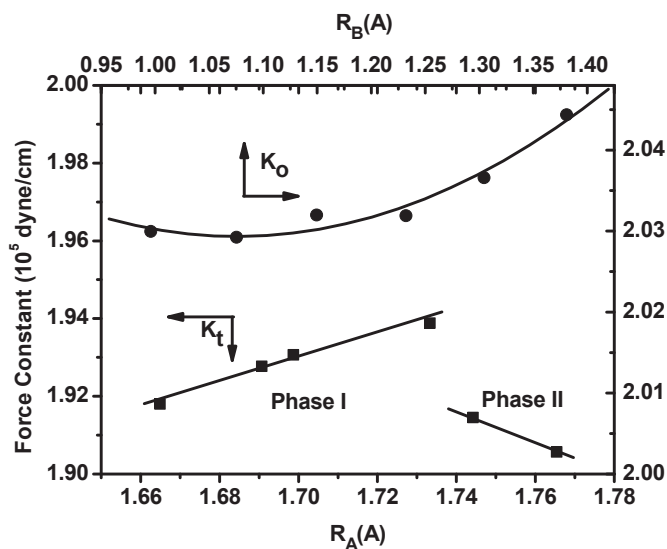


Fig. 19. The force constants  $K_t$  and  $K_o$  vs. bond lengths,  $R_A$  and  $R_B$  for the  $Mg_{1-x}Zn_xFeCrO_4$  spinels.

The ionic packing coefficients  $P_a$  and  $P_b$  at the tetrahedral and octahedral sites can be estimated using well known equations [18];

$$\left. \begin{aligned} P_a &= \frac{R_A - R_o}{r_A} \\ P_b &= \frac{R_B - R_o}{r_B} \end{aligned} \right\} \quad (10)$$

Where  $R_A$ ,  $R_B$ ,  $r_A$  and  $r_B$  are the average bond lengths and average ionic radii at the tetrahedral and octahedral sites and  $R_o$  is the  $O^{2-}$  ion radius. The small values of the packing factors,  $P_a$  and  $P_b$  are usually testify to the smaller ionic distances and larger overlapping of the cation and anion orbits, suggesting the existence of cation or anion vacancies [31]. Values of  $P_a$  and  $P_b$  for the  $Mg_{1-x}Zn_xFeCrO_4$  spinels are shown in Table 5 and Fig. 21. It is clear that values of  $P_a$  and  $P_b$  decrease with increasing  $Zn^{2+}$  content. Moreover,  $P_a$  decreases more strongly than  $P_b$ . These are indications of the

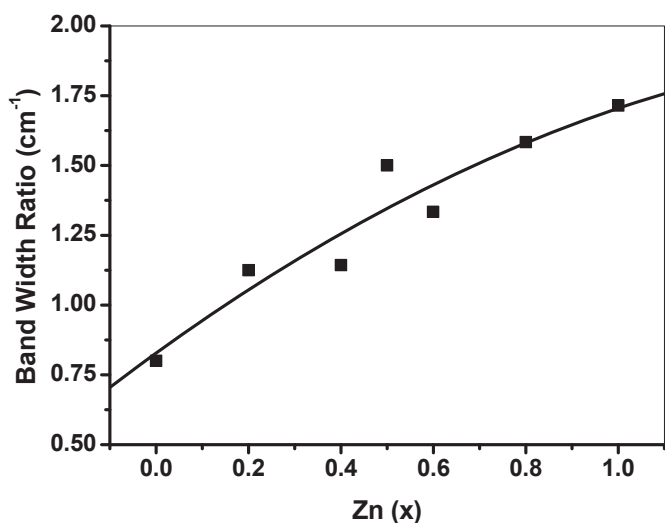


Fig. 20. The half bandwidth (HWMF) of  $\nu_1$  and  $\nu_2$  ratio vs.  $Zn(x)$  for the  $Mg_{1-x}Zn_xFeCrO_4$  spinels.

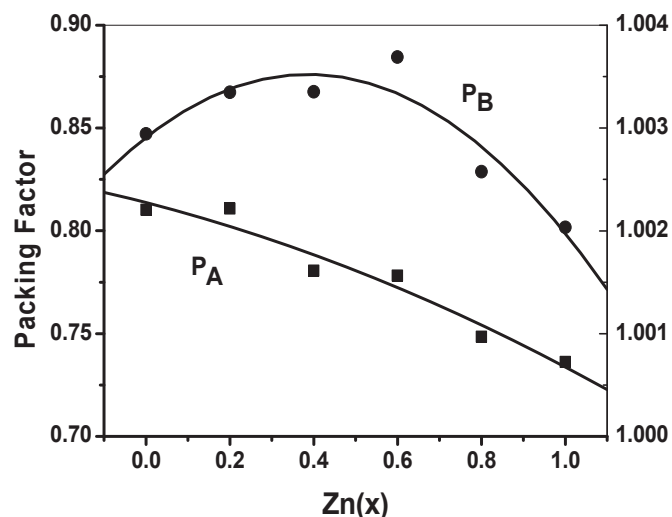


Fig. 21. The packing factors  $P_a$  and  $P_b$  vs.  $Zn(x)$  in the  $Mg_{1-x}Zn_xFeCrO_4$  spinels.

increased domination of the  $Zn^{2+}$  vacancies at the tetrahedral sites, playing the double acceptors role.

Moreover, the degree of the ionic packing of the spinel structure can be determined using the fulfillment coefficient of the unit cell,  $\alpha$ , which can be estimated using the following relation [17,31];

$$\alpha = \frac{32\pi}{3a_{exp}^3} (r_A^3 + 2r_B^3 + 4R_o^3) \quad (11)$$

Values of  $\alpha$  are shown in Table 5 and Fig. 22 as a function of  $Zn^{2+}$ . It is clear that values of  $\alpha$  fall in two distinct regions one belongs to the mixed inverse-normal spinel phase and the other for the normal spinel phase. It increases quite sharply at the boundary region between the two phases.

The total vacancy concentration existing in the sample,  $\beta$  can be estimated using the following equation [31];

$$\beta = \left( \frac{a_{th}^3 - a_{exp}^3}{a_{th}^3} \right) 100\% \quad (12)$$

Values of  $\beta$  are shown in Table 5 and Fig. 22. The  $\beta$  values increase slowly passing through broad maximum then decrease. The

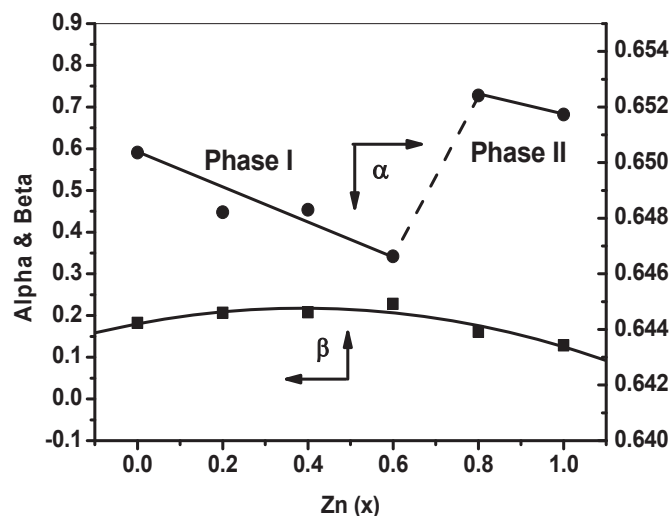


Fig. 22. The fulfillment coefficient,  $\alpha$  and total vacancy concentration,  $\beta$  vs.  $Zn(x)$  for the  $Mg_{1-x}Zn_xFeCrO_4$  spinels.

increase in  $\beta$  values indicates the presence of cation or anion vacancies. The slow increase can be considered as an indication of the gradual transition from the mixed spinel phase to the normal spinel phase. The other indication of the presence of vacancies at the tetrahedral and octahedral sites is the small values of the packing factors ( $P_a < 1$ ,  $P_b \sim 1$ ) and the fulfillment coefficient ( $\alpha < 1$ ). The jump in  $\alpha$  values can be taken as evidence of the domination of  $Zn^{2+}$  ions vacancies at the tetrahedral sites of the almost normal spinel phase, which might be the reason for the improvement of the electrical conductivity in the  $Zn^{2+}$  ions richest samples ( $x \geq 0.8$ ).

The electrical conductivity in ferrites was explained on the basis of the Verwey's mechanism, i.e. exchange of electrons between the adjacent  $Fe^{+2}$  and  $Fe^{+3}$  ions (and might be  $Cr^{3+}$  and  $Cr^{4+}$  ions) at the octahedral sites. Since the hopping mechanism is the most probable conduction mechanism in the Mg–Zn–Cr ferrites, the presence of the  $Zn^{+2}$  vacancies in these ferrites might play a considerable role for the improvement of the electrical conductivity (decrease in  $\rho$  values). These results agree with results of the thermoelectric power of the  $ZnCr_{2-x}Fe_2O_4$  [30] and the electrical conductivity in  $ZnCr_2O_4$  [31] and  $NiFe_2O_4$  [32] spinels, in which the presence of both negative and positive Seebeck coefficients were reported, suggesting that both n-type and p-type carriers are responsible for the conduction process in these materials. These processes can be explained by the following relations;



Similar role has been claimed for  $Zn^{+2}$  vacancies in the  $Mg_{1-x}Zn_xFe_2O_4$  [17] and  $ZnCr_{2-x}Ni_xSe_4$  [33] spinels.

The type of electrical conductivity and the magnetic spin state of the normal spinel ferrites have a distinct relation with their ionic packing factor at the tetrahedral and octahedral sites [19]. The  $Mg_{1-x}Zn_xFeCr_2O_4$  spinels are expected (on average) to be mixed inverse-normal spinels for ( $0.2 < x < 0.8$ ). The packing factors,  $P_a$  and  $P_b$  for these ferrites were calculated and found to be in the range (0.73–0.81) and (1.002–1.003) respectively. The  $P_a$  values lie at both sides of the border between the insulator–semiconductor conducting regions in the proposed classification. The measured values of the DC electrical conductivity of the  $Mg_{1-x}Zn_xFeCr_2O_4$  samples ( $\sim 10^{-9} \Omega^{-1}cm^{-1}$ ) support this classification. Moreover, the  $P_b$  values suggest that the ionic spins arrangements in these samples are antiparallel ferrimagnetic ordering at the B- sites according to the proposed classification. These predictions for the magnetic state have been supported by the Mossbauer results of the  $Mg_{1-x}Zn_xFeCr_2O_4$  spinels [5].

#### 4. Conclusions

The  $Mg_{1-x}Zn_xFeCrO_4$  spinels were prepared by the conventional solid state reaction method with double sintering at temperatures around 1100 °C. Detailed refinement analysis of the X-ray diffraction spectrum showed that these samples are a multiphase system, it is actually mixtures of pure  $MgFeCrO_4$  and Zn-doped  $MgFeCrO_4$  phases. Values of the lattice parameter, 'a' increase with  $Zn^{2+}$  content. The infrared spectra of these spinels give rise to two most prominent absorption bands. The high frequency band,  $\nu_1$  lies in the range between 602 and 625  $cm^{-1}$  was assigned to the  $Fe^{3+}-O^{2-}$  and  $Zn^{2+}-O^{2-}$  stretching vibrations at the tetrahedral sites. The low frequency band,  $\nu_2$  lies in the range between 491 and 497  $cm^{-1}$ , which is assigned to the  $Fe^{3+}-O^{2-}$ ,  $Cr^{3+}-O^{2-}$  and  $Mg^{2+}-O^{2-}$  stretching vibrations at the octahedral sites. The calculated values of the bond lengths  $R_A$  and  $R_B$ , ionic radii  $r_A$  and  $r_B$

and the force constants at the tetrahedral sites,  $K_t$  and the octahedral sites,  $K_o$  depend on the  $Zn^{2+}$  content. This behavior has been attributed to the variation in cation–oxygen bond length and the charge imbalance at the concerned sites. It can be concluded that the gradual increase of the  $Zn^{2+}$  content, x in the studied  $Mg_{1-x}Zn_xFeCrO_4$  spinel system leads to gradual transformation from the mixture normal-inverse to normal spinel structure. This transformation leads to the sharpening of the absorption bands. The room temperature DC electrical resistivity is of order ( $10^8-10^9$ )  $\Omega-cm$ . The increase of  $Zn^{2+}$  content lowers the resistivity in these ferrites. The ionic packing factors  $P_a$  and  $P_b$  and the vacancy parameter,  $\beta$  increase slowly. The fulfillment coefficient,  $\alpha$  parameter increases strongly as the  $Zn^{+2}$  content increase in the sample. The small values ( $<1$ ) of  $P_a$ ,  $P_b$ ,  $\alpha$  and  $\beta$  ( $\sim 1$ ) and the distortion of the spinel unit cell ( $u > 0.250$ ) form good evidences of the presence of cations or anions vacancies and for the phase transformation from the inverse-normal spinel to the normal spinel phase. The presence of vacancies in the  $Mg_{1-x}Zn_xFeCrO_4$  spinels might play (at least) partial role in the improvement of the electrical conductivity in these spinels.

#### References

- [1] V.G. Harris, A. Geiler, Y. Chen, S. Yoon, M. Wu, A. Yang, Z. Chen, P. He, P.V. Parimi, Xu Zuo, C.E. Patton, M. Abe, O. Acher, C. Vittoria, Recent advances in processing and applications of microwave ferrites, *J. Magn. Magn. Mater.* 321 (2009) 2035–2047.
- [2] A. Goldman, *Modern Ferrite Technology*, second ed., Springer Science Business Media, Inc., New York, 2006.
- [3] R. Valenzuela, *Magnetic Ceramics*, Cambridge University Press, 2005.
- [4] H. Kojima, in: E.P. Wohlfarth (Ed.), *Ferromagnetic Materials: A Handbook of the Properties of Magnetically Ordered Substances*, vol. 3, North-Holland, Amsterdam, 1982.
- [5] A.M. Gismelseed, K.A. Mohammed, M.E. Elzain, H.M. Widatallah, A.D. Al-Rawas, A.A. Yousif, Structural and magnetic studies of the Zn-substituted magnesium ferrite chromate, *Hyperfine Interact.* 208 (2012) 33–37.
- [6] M.C. Chhantbar, U.N. Trivedi, P.V. Tanna, H.J. Shah, R.P. Vara, H.H. Joshi, K.B. Modi, Infrared spectral studies of Zn-substituted  $CuFeCrO_4$  spinel ferrite system, *Indian J. Phys.* 78A (3) (2004) 321–326.
- [7] M.G. Brik, A. Suchocki, A. Kaminska, W. Paszkowicz, Lattice parameters and stability of the spinel compounds in relation to the ionic radii and electro-negativity of constituting chemical elements, *Inorg. Chem.* 53 (2014) 1–30.
- [8] R.D. Waldron, Infrared spectra of ferrites, *Phys. Rev.* 99 (1955) 1727–1735.
- [9] P.P. Hankare, V.T. Vader, U.B. Sankpal, L.V. Gavali, R. Sasikala, I.S. Mulla, Effect of sintering temperature and thermoelectric power studies of the system  $MgFe_{2-x}Cr_xO_4$ , *Solid State Sci.* 11 (2009) 2075–2079.
- [10] S.J. Haralkar, R.H. Kadam, S.S. More, S.E. Shirsath, M.L. Mane, S. Patil, D.R. Mane, Substitutional effect of  $Cr^{3+}$  ions on the properties of Mg–Zn ferrite nano particles, *Phys. B* 407 (2012) 4338–4346.
- [11] A. Globus, H. Pascard, V. Cagan, Distance between magnetic ions and fundamental properties in ferrites, *J. Phys. Colloq.* 38 (1977). C1-163–168.
- [12] S. Singhal, S. Bhukal, J. Singh, K. Chandra, S. Bansal, Optical, X-Ray diffraction, and magnetic properties of the cobalt-substituted nickel chromium ferrites ( $CrCo_xNi_{1-x}FeO_4$ ,  $x=0, 0.2, 0.4, 0.6, 0.8, 1.0$ ) synthesized using sol-gel auto combustion method, *J. Nanotechnol.* 2011 (2011) 1–6, <http://dx.doi.org/10.1155/2011/930243>. Article ID 930243.
- [13] A.K.M. Zakaria, M.A. Asgar, S.-G. Eriksson, F.U. Ahmed, S.M. Yunus, A.K. Azad, H. Rundlof, Preparation of Zn substituted Ni–Fe–Cr ferrites and study of the crystal structure by neutron diffraction, *Mater. Lett.* 57 (2003) 4243–4250.
- [14] K.J. Standley, *Oxide Magnetic Materials*, Clarendon Press, Oxford, 1990.
- [15] B.D. Cullity, *Elements of X-ray Diffraction*, Addison-Wesley, 1978.
- [16] R.J. Hill, J.R. Craig, G.V. Gibbs, Systematics of the spinel structure type, *Phys. Chem. Miner.* 4 (1979) 317–339.
- [17] K.A. Mohammed, A.D. Al-Rawas, A.M. Gismelseed, A. Sellai, H.M. Widatallah, A. Yousif, M.E. Elzain, M. Shongwe, Infrared and structural studies of  $Mg_{1-x}Zn_xFe_2O_4$  ferrites, *Phys. B* 407 (2012) 795–804.
- [18] B.F. Levine, d-Electron effects on bond susceptibilities and ionicities, *Phys. Rev. B* (1973) 2591.
- [19] T. Satoh, T. Tushima, K. Kudo, A classification of normal spinel type compounds by "ionic packing factor", *Mater. Res. Bull.* 9 (1974) 1297–1300.
- [20] G.K. Williamson, W.H. Hall, X-ray line broadening from filed aluminum and wolfram, *Acta Metall.* 1 (1953) 22–31.
- [21] S.M. Patange, S.E. Shirsath, B.G. Toksha, S.S. Jadhav, K.M. Jadhav, Electrical and magnetic properties of  $Cr^{3+}$  substituted nanocrystalline nickel ferrite, *J. Appl. Phys.* 106 (2009), 023914-1-7.
- [22] M. Chakrabarti, D. Sanyal, A. Chakrabarti, Preparation of  $Zn_{1-x}CdxFe_2O_4$  ( $x = 0.0, 0.1, 0.3, 0.5, 0.7$  and  $1.0$ ) ferrite samples and their characterization by Mössbauer and positron annihilation techniques, *J. Phys. Condens. Matter.* 19

- (2007) 236210 (11pp).
- [23] S.S. Khot, N.S. Shinde, B.P. Ladgaonkar, B.B. Kale, S.C. Watawe, J. Adv. Appl. Sci. Res. 460 (2011) 460–471.
- [24] M.V. Kuznetsov, Q.A. Pankhurst, I.P. Parkin, Self propagating high-temperature synthesis of chromium substituted magnesium zinc ferrites  $Mg_{0.5}Zn_{0.5}Fe_{2-x}Cr_xO_4$  ( $0 \leq x \leq 1.5$ ), J. Mater. Chem. 8 (1998) 2701–2706.
- [25] S. Bhukal, T. Namgyal, S. Mor, S. Bansal, S. Singhal, Structural, electrical, optical and magnetic properties of chromium substituted Co–Zn nanoferrites  $Co_{0.6}Zn_{0.4}Cr_xFe_{2-x}O_4$  ( $0 \leq x \leq 1.0$ ) prepared via sol–gel auto-combustion method, J. Mol. Struct. 1012 (2012) 162–167.
- [26] L.B. Tahar, H. Basti, F. Herbst, L.S. Smiri, J.P. Quisefit, Y. Yaacoub, J.M. Greneche, S. Ammar,  $Co_{1-x}Zn_xFe_2O_4$  ( $0 \leq x \leq 1$ ) nanocrystalline solid solution prepared by the polyol method: Characterization and magnetic, Mater. Res. Bull. 47 (2012) 2590–2598.
- [27] S.A. Mazen, A.M. AlTaher, The conduction mechanism of Cu–Ge ferrite, Solid Stat. Commun. 150 (2010) 1719–1724.
- [28] M.L.S. Teo, L.B. Kong, Z.W. Li, G.Q. Lin, Y.B. Gan, Development of magneto-dielectric materials based on Li-ferrite ceramics: II. DC resistivity and complex relative permittivity, J. Alloys Comp. 459 (2008) 567–575.
- [29] S.J. Yoon, S.H. Lee, K.H. Kim, K.S. Ahn, Electrical and magnetic properties of spinel  $ZnCr_{2-x}Fe_xO_4$  ( $0 \leq x \leq 1.0$ ), Mater. Chem. Phys. 73 (2002) 330–334.
- [30] T.T. Srinivasan, C.M. Srivastava, N. Venkataramani, M.J. Patni, Infrared absorption in spinel ferrites, Bull. Mater. Sci. 6 (1984) 1063–1067.
- [31] T. Gron, Influence of vacancies and mixed valence on the transport processes in solid solutions with the spinel structure, Philos. Mag. B 70 (1994) 121–132.
- [32] S. Anjum, G.H. Jaffari, A.K. Rumaiz, M.S. Rafique, S.I. Shah, Role of vacancies in transport and magnetic properties of nickel ferrite thin films, J. Phys. D: Appl. Phys. 43 (2010), 265001-7.
- [33] H. Duda, I. Jendrzewska, T. Gron, S. Mazur, P. Zajdel, A. Kita, Influence of vacancies on the electrical properties of the  $ZnCr_{2-x}Ni_xSe_4$  spinels, J. Phys. Chem. Solids 68 (2007) 80–86.